AGU PUBLICATIONS

JGR

Journal of Geophysical Research: Oceans

RESEARCH ARTICLE

10.1002/2017JC013370

Surface Wave Dynamics in Delaware Bay and Its Adjacent Coastal Shelf

Tobias Kukulka[1], Robert L. Jenkins III[1], James T. Kirby[2], Fengyan Shi[2], and Robert W. Scarborough[3]

[1]School of Marine Science and Policy, University of Delaware, Newark, DE, USA, [2]Center for Applied Coastal Research, University of Delaware, Newark, DE, USA, [3]Delaware Department of Natural Resources and Environmental Control, Dover, DE, USA

Key Points:
- Energetic surface gravity waves are dominantly swell on the shelf and wind-driven waves in the bay
- Bathymetric refraction shelters the bay from energetic surface gravity waves from the shelf
- Strong tidal currents refract waves and focus wave energy near the bay entrance

Correspondence to:
T. Kukulka,
kukulka@udel.edu

Citation:
Kukulka, T., Jenkins, R. L., Kirby, J. T., Shi, F., & Scarborough, R. W. (2017). Surface wave dynamics in Delaware Bay and its adjacent coastal shelf. *Journal of Geophysical Research: Oceans*, *122*. https://doi.org/10.1002/2017JC013370

Received 18 AUG 2017
Accepted 7 OCT 2017
Accepted article online 13 OCT 2017

Abstract This study presents a broad overview of surface gravity wave dynamics in Delaware Bay and the adjacent continental shelf by employing the wave model Simulating Waves Nearshore one-way coupled to the ocean model Regional Ocean Modeling System for a period from 2006 to 2012. The distributions of simulated wave statistics agree well with observations obtained from three wave buoys located on the shelf, in the bay near the open ocean, and about 35 km up the bay. A partitioning analysis to separate the two-dimensional wave height spectrum into wind-forced and swell parts reveals that waves on the shelf are predominantly remotely generated swell. Bathymetric refraction shelters the bay from energetic open ocean waves, which is supported by an idealized ray tracing analysis. Waves near the bay entrance are also refracted by oblique tidal currents, whose refraction characteristics critically depend on the detailed spatial distributions of the currents. Opposing tidal currents, flowing against the wave propagation direction, focus wave energy outside the bay entrance and in the deeper bay channels, where currents are relatively strong. A spectral partitioning analysis for waves in the bay indicates that less energetic wave fields are likely not directly forced by the wind. More energetic waves, on the other hand, are dominantly driven by winds and the wave response in the bay depends on the fetch-setting wind direction. Our results for wind-driven waves in the bay are consistent with previous fetch-limited observations, but we find a systematic bias between wind and wave directions due to bathymetric refraction.

1. Introduction

Delaware Bay and its adjacent coastal shelf support one of the world's most densely populated regions and uniquely rich ecosystems (Baker et al., 2004; Botton et al., 1988; Hofmann et al., 2009). Extensive changes in the Delaware Bay coastline have been observed with coastline erosion rate estimates ranging from about 0.1 to 1 m/yr (Kraft et al., 1992; Phillips, 1986; Pijanowski & Sommerfield, 2015). Coastal surface gravity waves play a critical role in such geomorphological changes, e.g., by controlling sediment transport (Longuet-Higgins, 1953; Trowbridge & Madsen, 1984) and wave setup (Longuet-Higgins & Stewart, 1964). More recently, it has been established that surface gravity waves also drive coastal currents (Lentz & Fewings, 2012; McWilliams et al., 2004) and control turbulent transport processes (Gargett et al., 2004; Gerbi et al., 2009; Kukulka et al., 2012; Scully et al., 2015). The goal of this study is to provide a broad overview of surface gravity wave dynamics in Delaware Bay and its adjacent continental shelf.

Significant observational, theoretical, and modeling progress have been made over the last several decades in understanding the dynamics of surface gravity waves in the open ocean, on the shelf, and in nearshore environments (see, e.g., the comprehensive reviews by Phillips (1977), Komen et al. (1996), Mei et al. (2005), Cavaleri et al. (2007), and Holthuijsen (2010)). In environments with slowly varying depth and ocean currents, the evolution of surface gravity waves is governed by the conservation of spectral wave action, which changes due to source terms associated with wind input, nonlinear wave-wave interactions, and dissipation of wave energy usually due to wave breaking. For steady winds, the wave field equilibrates with the wind forcing, resulting in a balance between all three source terms, which is referred to as wind-wave equilibrium sea state (Phillips, 1958, 1985). Limited duration and fetch of the wind forcing reduce the wave growth to decrease wave heights and periods (Donelan et al., 1985; Hasselmann et al., 1973; Romero & Melville, 2010; Young &

Verhagen, 1996). If the wind subsides or faster longer waves propagate out of the wind-wave generation region, ocean waves travel as relatively long-period swell waves over great distances across the ocean basin to enter coastal regions (Ardhuin et al., 2009; Hanley et al., 2010; Munk et al., 1963; Semedo et al., 2011).

In principle, the physics that govern the evolution of surface gravity waves in coastal regions are similar to those in open ocean environments, with the source terms modified for a depth-limited ocean (Cavaleri et al., 2007; Holthuijsen, 2010; Komen et al., 1996; Mei et al., 2005; Phillips, 1977). For example, nonlinear triad wave-wave interactions become important in shallow-water, and wave dissipation is affected by interactions with the bottom. In addition, variable bathymetry, obstructing coastlines, and strong tidal currents influence wave propagation in coastal oceans. The presence of coastlines leads to fetch-limited conditions if the wind blows offshore (Donelan et al., 1985; Hasselmann et al., 1973; Romero & Melville, 2010; Young & Verhagen, 1996). Shallow depths slow down wave propagation to cause wave shoaling, steepening, and associated depth-induced breaking (e.g., Elgar & Guza, 1985; Herbers & Burton, 1997). Varying bathymetry also leads to wave refraction, focusing, or spreading wave energy (e.g., Ardhuin et al., 2009; Herbers et al., 2000). Similarly, sheared horizontal currents result in current-induced refraction (e.g., Johnson, 1947; Smith, 1976). Spatially varying opposing currents, flowing against the wave propagation direction, cause wave steepening analogous to a shoaling bathymetry (e.g., Peregrine, 1976; Tolman, 1990). Collinear currents also Doppler shift the wave frequency.

By employing a spectral wave model and by analyzing wave observations, the goal of this paper is to provide a broad, yet systematic, overview of typical wave characteristics in Delaware Bay and its adjacent coastal shelf. Building on previous approaches, the model is designed as a straightforward research tool that allows a systematic assessment of the role of wind-driven waves, swell, refraction, current effects, and the exchange of wave energy between bay and shelf. Observations are used to validate the distributions of simulated wave statistics and the wave response to the forcing and environment. An in-depth direct comparison between observations and simulations, whose success greatly depends on the quality of the applied boundary forcing, such as spatiotemporally varying wind vectors, is beyond the scope of this study. The following section describes the model approach and observations. Section 3 discusses first wave results on the shelf and then in the bay. The paper concludes with a discussion in section 4.

2. Methods

Our model design philosophy is to build on previous approaches, employ common (default) model parameters without tuning, and apply readily accessible forcing fields. The model simulations are for a time period when wave observations in the bay and on the shelf are readily available.

2.1. Coupled Wave Ocean Model

2.1.1. Previous Ocean Models for Delaware Bay

Significant progress has been made over the last decade in modeling the ocean circulation in and near Delaware Bay. The modeling study by Whitney and Garvine (2005, 2006) identified the influences of winds, tides, and river discharge on buoyant plume dynamics and associated currents near the shelf. In this study, we use an advanced version of the Whitney and Garvine model, which improves the model forcing (Castellano & Kirby, 2011; Jenkins, 2015). Similar circulation models have been applied successfully in previous process studies, for example, to investigate the role of offshore wind conditions on Delaware plume dynamics (Jurisa & Chant, 2013), to understand the influence of secondary circulations on net salt fluxes (Aristizábal & Chant, 2013), and to model distributions of larval bivalves (Hofmann et al., 2009). The ocean modeling systems for the US Middle Atlantic Bight ("ESPRESSO" model, Zavala-Garay et al., 2014) and the Delaware River and Bay ("DBOFS" model, Schmalz, 2011) provide operational forecasts. Generally, these simulations are consistent with the observed relatively strong tidal currents near the entrance of Delaware Bay, which are dominated by M2 tides with maximum amplitudes of about 0.9 m/s near the surface where the channel is deep (Münchow et al., 1992). On the continental shelf, coastal currents are weaker and driven by wind stress and buoyancy due to the presence of the Delaware River plume (Whitney & Garvine, 2005, 2006; Wong & Münchow, 1995). Remote oceanic disturbances that are generated outside the study area, e.g., by remote storms, may also force the regional ocean circulation (Rodrigues, 2016), but such remote forcing is not considered in this study.

In comparison to ocean circulation models, realistic wave models for Delaware Bay and its adjacent coastal shelf are less advanced. Qin et al. (2005) employed a spectral wave model to assess the sensitivity of

simulations on forcing conditions and to identify wave modulations due to currents. A coupled wave-ocean model has been deployed to investigate storm surge, waves, and coastal inundation in the region under idealized tropical cyclone conditions (Chen et al., 2008). Chen et al. (2016) utilized a similar coupled wave-ocean model in an effort to examine the recent loss of salt marshes at the western shore of Delaware Bay.

2.1.2. Modeling Framework

The model used in this study is based on a coupled application of the Regional Ocean Modeling System (ROMS, Haidvogel et al., 2000; Shchepetkin & McWilliams, 2005) and Simulating Waves Nearshore (SWAN, Booij et al., 1999; SWAN Team, 2007, 2009) within the Coupled-Ocean-Atmospheric-Wave-Sediment Transport (COAWST) modeling framework (Warner et al., 2010). Recently, similar modeling systems have been successfully applied to investigate the wave and circulation dynamics of the mouth of the Columbia River (Akan et al., 2017) and of the midshelf to surfzone of the US West Coast (Kumar et al., 2015).

Our computational domain is the same as in Whitney and Garvine (2006) and encompasses the full Delaware Bay, parts of the upper estuary, and a portion of the nearby coastal region (Figure 1). The grid is regular curvilinear with highest grid resolution near the bay mouth at 0.75–2.0 km and lowest grid resolution near the shelf break with a grid spacing of about 8 km. This relatively coarse spatial resolution is consistent with the spatial resolution of previous ocean models, which have successfully simulated ocean currents (Castellano & Kirby, 2011; Jenkins, 2015; Whitney & Garvine, 2005, 2006). Furthermore, similarly coarse

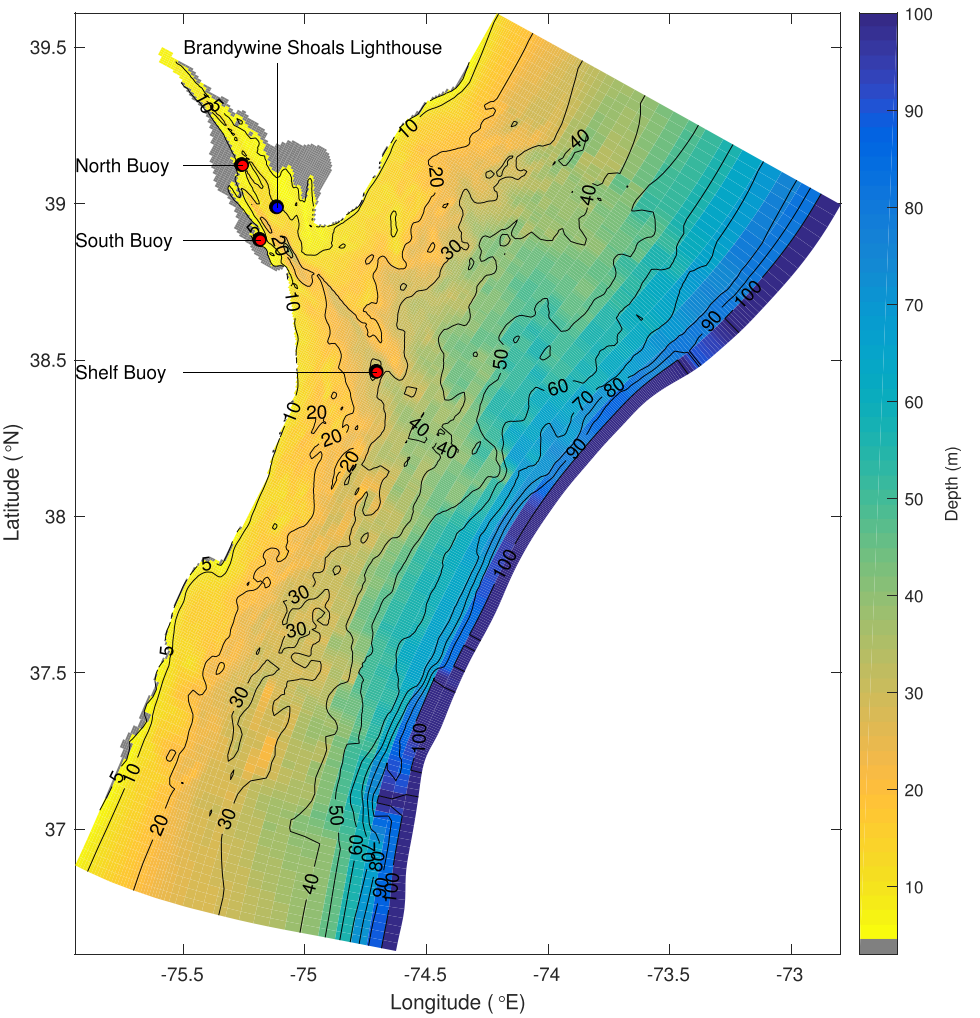

Figure 1. Model bathymetry and domain. Wave buoy observation stations (red dots) include the North Buoy (NDBC station 44055) and South Buoy (NDBC station 44054) in Delaware Bay and the Shelf Buoy (NDBC station 44009) on the shelf. Station Brandywine Shoals Lighthouse (NDBC station BRND1) provides meteorological observations (blue dot). The eastern, northern, and southern boundaries of the domain are open ocean boundaries.

resolutions have been employed successfully in earlier coastal wave studies (see, e.g., reviewed by Holthuijsen (2010)), and our results show that our wave model resolves adequately many key wave characteristics. The coast extends from just south of the Chesapeake Bay mouth (37.00°N, −75.96°E) to just south of Ship Bottom, New Jersey (39.65°N, −74.18°E). Chesapeake Bay and barrier island inlets along the coast are not resolved and are not the focus of this study. The ocean component of our model has been previously validated, and accurately captures buoyancy-driven coastal currents (Whitney & Garvine, 2005, 2006) and tidal currents in the bay and near the coast (Castellano & Kirby, 2011; Jenkins, 2015).

2.1.3. Wind Forcing

Both the ocean circulation and wave models are forced by spatially and temporally varying winds, which are estimated from the reanalysis data product North American Mesoscale (NAM) (nomads.ncdc.noaa.gov). NAM wind vectors are obtained at 12 km resolution every 6 h and interpolated to the finer Delaware Bay. Wind speeds are converted to surface stresses based on a log profile and drag coefficients from Large and Pond (1981) to force the circulation model. The wind velocity vector varies significantly spatially and seasonally (Figure 2). Notably, wind speeds in the bay are lower than on the shelf. Lowest winds occur in the summer months and blow primarily from the south-west. During winter, wind speeds are largest and the wind direction is approximately from the north-west. Spring and autumn months in the record show moderate wind speeds with greater directional variability.

2.1.4. Lateral Boundary Conditions

Lateral boundary conditions for both the ocean circulation and wave model need to be imposed. For ROMS, northern, eastern, and southern boundaries are open, while the western boundary is closed and treated as a wall with free-slip conditions for tangential velocities and a zero-gradient for surface and tracers

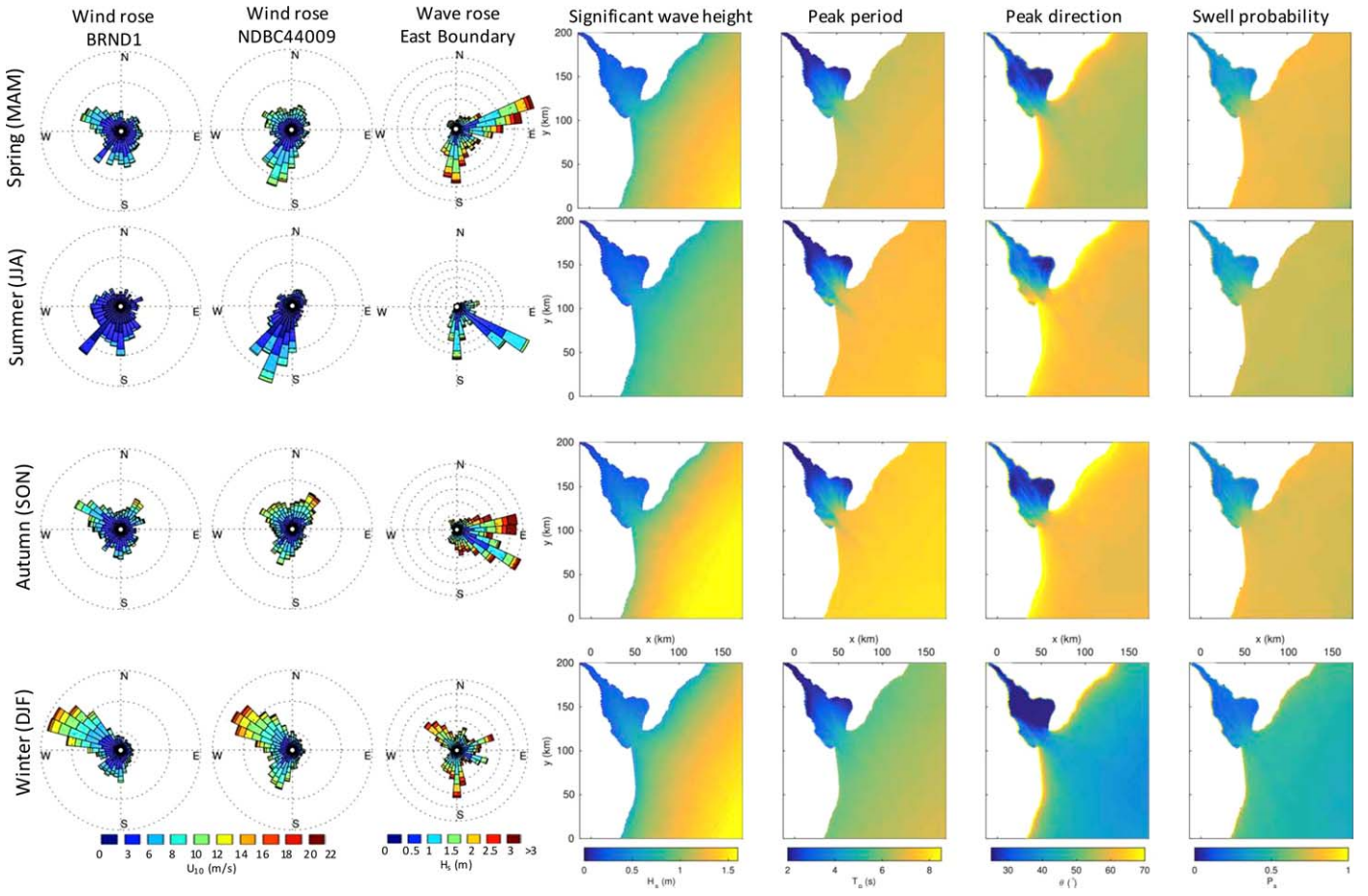

Figure 2. Seasonal NAM wind roses in the bay at station BRND1 (first column) and offshore at station NDBC 44009 (second column), and seasonal WaveWatchIII significant wave height and peak wave direction at an eastern boundary location (third column). Seasonal means for modeled wave variables: H_s (fourth column), T_p (fifth column), misalignment angle between wind and waves θ (sixth column), and swell probability P_s (seventh column) for the 7 year simulation period.

following Castellano and Kirby (2011). SWAN is forced at the open boundaries by hourly archived WaveWatchIII wave data of significant wave height, peak period, and peak wave direction (polar.ncep.noaa.gov/waves). Consistent with the WaveWatchIII 4 arc-minute coastal grid for the US East Coast used in this study, we divide each of the three open ocean boundaries into three segments over which wave boundary conditions are constant along each segment. Waves imposed at the boundaries propagate into the modeling domain and are hence remotely generated. Boundary waves are from a range of directions between north-east and south at periods of 6–12 s with wave heights between 0.5 and 3.5 m and are characterized by seasonal variability (Figure 2). During spring months, waves travel from the north-east and south, while waves propagate from the south and south-east during summer at small wave heights. During autumn, waves mainly propagate from north-east and south-east. The winter months show the highest directional variability with some of the smallest period waves traveling from the north-east.

2.1.5. Tides and Freshwater Input

ROMS is also forced by realistic tides and river point source forcing for daily freshwater volume flux at the farthest upstream location. Discharge volumes are derived from USGS daily stream gauge observations collected at Trenton, New Jersey (waterdata.usgs.gov). The Delaware River discharge at Trenton is estimated to account for 58% of total freshwater input with an average discharge of 350 m^3/s (Sharp, 1983) and imposed discharge values are scaled accordingly to account for other freshwater sources (Castellano & Kirby, 2011; Sharp, 1983). The freshwater source is imposed at an artificial Delaware River extension (not shown in Figure 1) to mix more realistically river and ocean water as fresher water enters the upper bay (Castellano & Kirby, 2011). Following the approach of Castellano and Kirby (2011), tidal forcing in the ROMS model is handled with realistic tidal constituents, including M2, S2, M4, M6, K2, K1, N2, O1, and Q1. Amplitude and phases for these nine tidal constituencies have been taken from the ADCIRC tidal database (Luettich et al., 1992) and are imposed at the open boundaries.

2.1.6. Additional Details

The coupled model is run for a period from 1 January 2006 to 31 December 2012. ROMS calculations are resolved in time steps of 150 s, while the SWAN computational time step is 900 s. Every 1800 s, ROMS output of surface height (depth) and depth averaged horizontal currents is passed to SWAN (one-way coupling) based on the approach by Kirby and Chen (1989). Vertical resolution varies according to the depth and bathymetry based on terrain following coordinates that are vertically stretched with higher resolution near the air-sea interface (Shchepetkin & McWilliams, 2005). Ten depth layers are specified in ROMS. The wave frequency resolution in the SWAN model is logarithmically spaced from 0.04 to 1 Hz with 21 frequency bins. Our results indicate that this frequency range is usually adequate in this study to resolve the energy containing range of waves. Note also that simulating waves at higher frequencies is associated with significant uncertainties in parameterizing the source terms (e.g., Hara & Belcher, 2002; Kukulka & Hara, 2008). The wave directional resolution in the SWAN model is spaced equally into 36 directional bins each spanning 10°, which is sufficient to capture turning wave rays in the refracting Delaware Bay environment. A series of sensitivity tests to examine time, wave frequency, and directional resolution indicate that the chosen numerical resolution yields robust numerical solutions (e.g., doubling the frequency and direction resolution changed integrated wave parameters by less than 1%). The ocean model is spun up for several months, so that the initial condition does not affect the numerical solutions analyzed here.

The ocean circulation model does not receive input from the wave model in this study, although waves influence the ocean circulation through, e.g., Stokes drift advection, Stokes-Coriolis acceleration (Hasselmann, 1970), Craik-Leibovich vortex force (Craik & Leibovich, 1976) and through controlling upper ocean turbulence by wave breaking (Melville, 1996), and Langmuir circulations (Thorpe, 2004). Accurately representing those wave effects in Reynolds-averaged circulation models is an ongoing research effort (e.g., Lentz & Fewings, 2012; McWilliams et al., 2004; Mellor, 2008; Smith, 2006; Sullivan & McWilliams, 2008; Umlauf & Burchard, 2003) and not addressed here, consistent with the objectives of this paper.

2.2. Observations

2.2.1. Waves

The Delaware Coastal Management Program of the Delaware Department of Natural Resources and Environmental Control deployed two moored TRIAXYS directional wave buoys in the bay (Brown & Scarborough, 2013). One buoy was located in the central Delaware Bay about 35 km from the bay entrance in 7 m deep water (National Data Buoy Center [NDBC, ndbc.noaa.gov] station number 44055, Figure 1). This buoy, referred to as North Buoy or North Bay in this study, was deployed during June 2007 to February 2012, with major data gaps from July 2009 to May 2010 and January–May 2011. The second buoy, here referred to as South Buoy or South

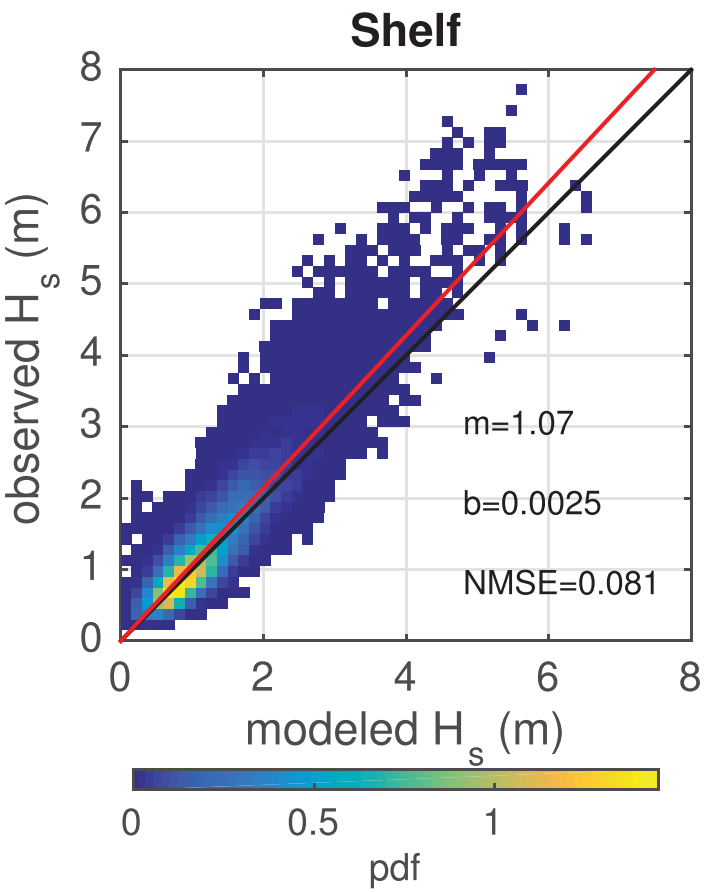

Figure 3. Linearly scaled probability density function (pdf) of observed H_s ($H_{s,o}$) versus modeled ($H_{s,m}$) for all available data between 2006 and 2012 at NDBC 44009 (Shelf), 1:1 line (black), and linear regression fit $H_{s,o}=mH_{s,m}+b$ (red line, units of b are in meter).

Bay, was deployed in the lower Delaware Bay near the bay entrance in 8 m deep water during October 2007 to October 2009 with a major data gap during April and July 2008 (NDBC station 44054, Figure 1).

The raw data from the buoy accelerometers, angular rate sensors, and compass are sampled at 4 Hz and postprocessed using a TRIAXYS software package, which includes a directional wave analysis based on cross-spectra between horizontal and vertical buoy motion. Postprocessed hourly wave statistics includes key wave parameters such as significant wave height, H_s, peak wave period, T_p, peak direction θ_p, and the one-dimensional and two-dimensional wave height frequency spectra, $\phi_1(f)$ and $\phi_2(f,\theta)$, respectively, where θ is the wave propagation direction. The measured wave frequency, f, ranges from 0.64 to 0.03 Hz with 123 bins of 0.05 Hz width. Note that care must be taken in interpreting the measured low-frequency content because accelerometer noise is weighted by f^{-4} in the wave height spectrum, resulting in spurious low-frequency wave energy.

We also analyze wave buoy observations from NDBC station 44009 on the shelf (Shelf Buoy, Figure 1), about 50 km south-east of the Delaware Bay entrance in 43 m depth. This buoy is owned and maintained by NDBC, so that measurement and quality control procedures follow the standard NDBC protocol. Although directional wave information was not available during the simulation period from 2006 to 2012, other common wave statistics, such as ϕ_1, are invaluable to validate the model.

2.2.2. Wind

To examine the observed wave response to wind forcing and also to assess the limitations of the NAM wind product, we analyze wind observations in the bay and on the shelf, which are provided by the National Oceanic and Atmospheric Administration (NOAA, http://www.ndbc.noaa.gov). The meteorological station in the bay, NDBC station BRND1, is located inside the bay about 15 km from the bay entrance (Figure 1). On the shelf, wind vectors are observed at NDBC station 44009 (Figure 1).

The wind speed at 10 m height, U_{10}, obtained from the NAM product is consistent with measurements at NDBC station 44009 with normalized mean square error NMSE = 0.07 and b = 0.68 m/s, and m=0.89 for the regression $U_{10}[NDBC]=mU_{10}[NAM]+b$. As expected, NAM winds agree less with measured wind fields in the bay due to small-scale spatiotemporal variability (Hughes & Veron, 2015). For example, for winds near station BRND1 (Figure 1), we find NMSE = 0.22, b= 2.12 m/s, and m = 0.92. Thus, although NAM winds are useful for a statistical comparisons between observations and simulations and allow an objective investigation of wave physics, the errors in NAM winds need to be taken into account, in particular for any direct comparison between observations and simulations.

3. Results

3.1. Wave Dynamics on the Shelf

3.1.1. Overview

To provide first an overview of wave statistics on the shelf in response to seasonal forcing, we group our wave results in spring (MAM), summer (JJA), autumn (SON), and winter (DJF) seasons (Figure 2). Based on our 7 year wave simulation, we examine basic seasonal statistics of significant wave height (H_s), peak period (T_p), absolute misalignment angle between wind and waves ($|\Delta\theta_p|$), and swell probability (P_s).

The significant wave height is defined as four times the standard deviation of the surface elevation. For all seasons, mean H_s on the shelf is larger offshore because of the larger fetches and stronger winds on the shelf. Although winds are strongest during winter, the largest H_s occur in autumn. This is because remotely generated swell waves have larger amplitudes during autumn. Smallest H_s values occur in summer, as wind

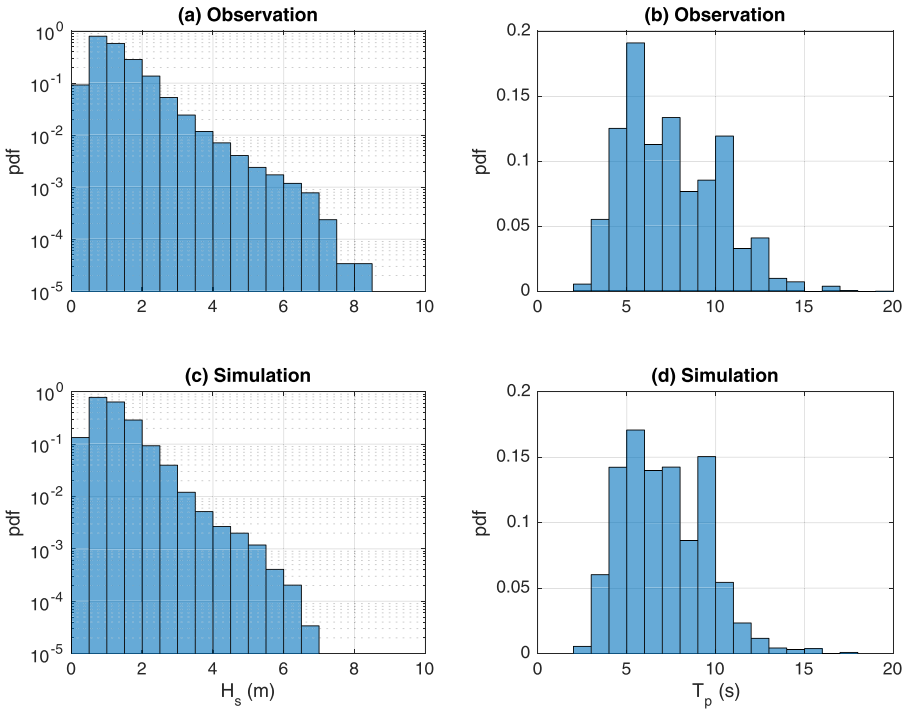

Figure 4. Probability density function (pdf) of (a, b) observed and (c, d) simulated significant (a, c) wave height and (b, d) peak period at NDBC 44009 (Shelf).

and wave boundary forcing are weakest for this season. Summer mean H_s values on the shelf are between 0.75 and 1.25 m.

The peak period T_p is defined as the inverse of the wave frequency at the spectral peak. Lowest T_p occurs during winter and highest T_p during autumn months with values on the shelf of 6.5 and 8 s, respectively (Figure 2). Larger periods in autumn are again associated with especially strong remote swell forcing. Smaller offshore T_p for the winter indicates younger wind-driven seas at those locations, which is consistent with winter H_s and the wind and wave boundary forcing. Contrary to expectations based on wind forcing, for the summer months, the smallest T_p on the shelf does not occur in summer because of long period remotely generated swell with relatively small wave heights. Spring T_p on the shelf are moderate, similar to H_s, with values around 6.5 s.

The absolute misalignment angle between wind and waves, $|\Delta\theta_p|$, is defined as the absolute difference between the wind and spectral peak wave directions. For wind-driven seas, $|\Delta\theta_p|$ is close to zero. In the presence of swell, wind and peak wave direction may be significantly misaligned and $|\Delta\theta_p|$ approaches 180° for opposing wind and peak wave directions. For all seasons, mean $|\Delta\theta_p|$ on the shelf are on average less than 90° but larger than 45° throughout most of the domain, suggesting the presence of swell-driven waves on the shelf (Figure 2).

The swell probability P_s, which is defined by the number of instances of swell over the total number of instances in the record, is consistent with the distribution of $|\Delta\theta_p|$. Here an instance is counted as swell if the wave age, $c_p/[U_{10}\cos(|\Delta\theta_p|)]$, exceeds 1.2 ($c_p$ is the phase velocity at T_p), or $|\Delta\theta_p|$ is greater than 90° (Hanley et al., 2010). The spring, summer, and autumn seasons have similar values on the shelf with $P_s > 70\%$. Swell probability is lower in the winter than for the other seasons with values on the shelf at about 50%. This is consistent with our previous seasonal results, which indicated primarily wind-driven seas during winter.

3.1.2. Comparison of Observations and Simulations

We compare observed H_s to simulations for the 7 year period at the Shelf location (NDBC 44009) (Figure 3). The linear regression line between observations and simulations is indicated by the red line with slope *m*, *y*-intercept *b*, and the normalized mean squared error (NMSE) between observations and simulations is also shown. The regression slopes and *y*-intercepts are close to one and zero, respectively, indicating that

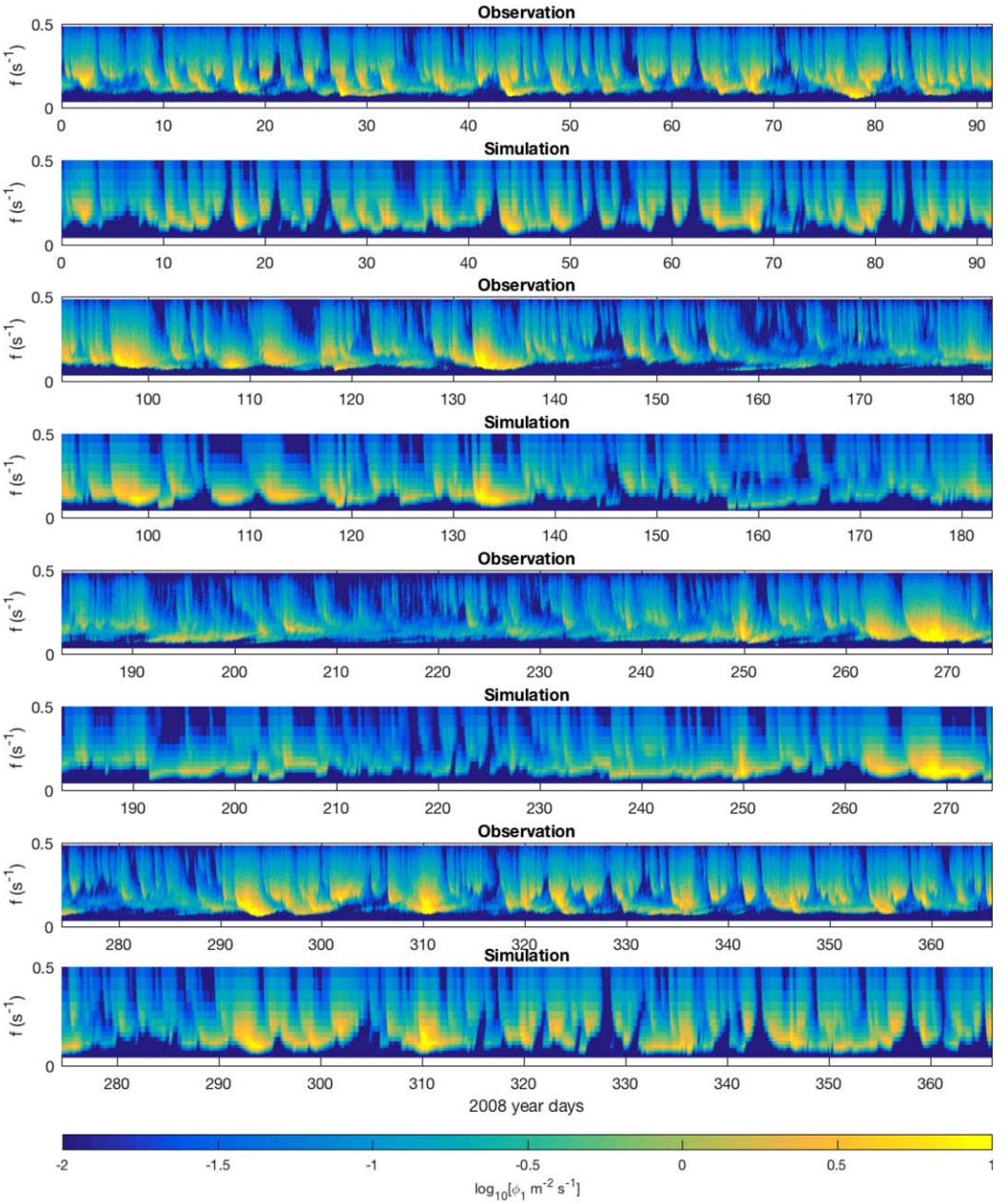

Figure 5. Observed and simulated one-dimensional wave height spectrum $\phi_1(f)$ in 2008 at NDBC 44009 (Shelf).

modeled and observed H_s agree reasonably well. The NMSE values are consistent with uncertainties in the wind forcing discussed earlier. Note also that the NAM wind for the simulations as only 12 km resolution.

The observed and simulated probability density functions (pdfs) of H_s and T_p agree surprisingly well (Figure 4) given that the model has not been optimized to enhance the agreement and the known shortcomings of the wind and wave data used to drive the simulations. For $H_s < 4$ m, H_s distributions agree well both qualitatively and quantitatively. Large H_s events with $H_s > 4$ m, however, are more challenging to model because accurate simulations depend on extreme events imposed through the boundary conditions. The observed and simulated pdfs of T_p show a peak around 6 s and relatively few T_p values at intermediate periods of just below 9 s, which indicates a separation between wind-driven and long-period swell waves as discussed below. The peak swell period is between 9 and 11 s. The presence of longer period swell waves with $T_p > 11$ s or shorter period waves with $T_p < 2$ s is unlikely. The most likely T_p occurs between 4 and 8 s, which is in the range of typical wind-driven seas.

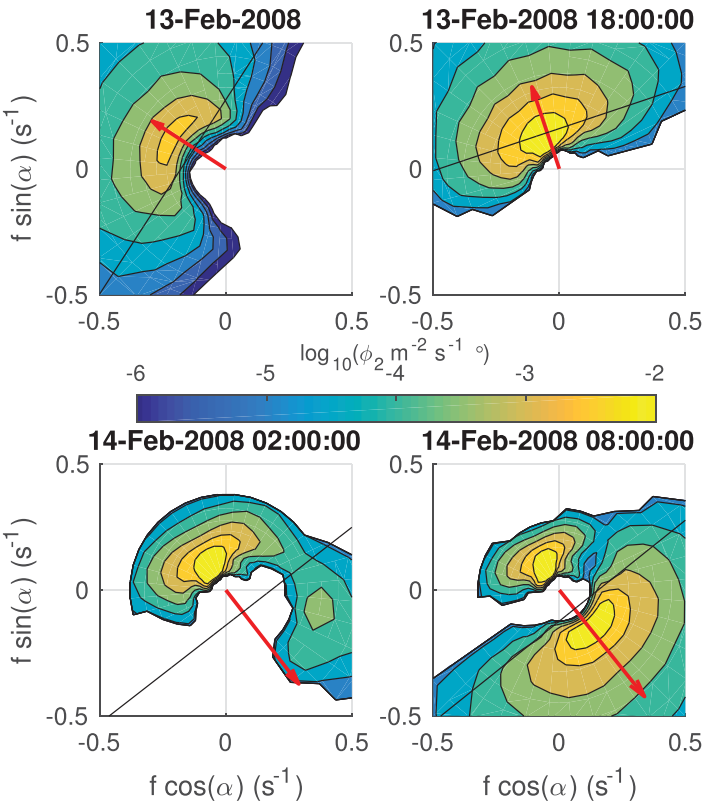

Figure 6. Example of simulated two-dimensional wave height spectrum $\phi_2(f,\theta)$ at NDBC 44009 (Shelf) in response to a turning wind event. The black line separates the wind-forced part of the spectrum for which $c/[U_{10}\cos(\Delta\theta)] \leq 1.2$, where $c(f)$ is the phase speed and $\Delta\theta$ is the difference between wind direction and θ. The red line indicates the wind vector, its maximum length corresponds to $U_{10}=13.5$ m/s. The wave propagation direction angle $\alpha=270^\circ-\theta$ uses Cartesian convention.

Consistently, simulated and observed time-dependent one-dimensional wave height frequency spectra $\phi_1(f)$ agree well (Figure 5, spectra shown for year 2008), where f is the wave frequency (inverse period) and $\langle\eta^2\rangle = \int_0^\infty \phi_1(f)df$ is the mean squared sea surface displacement height (η). Note that observations of two-dimensional wave height spectra were not available during the study period. In spite of shortcomings in the wind forcing and lateral wave boundary conditions, the simulations capture many detailed quantitative and qualitative features of the observations. For example, the model reproduces observed frequency downshifts for developing seas (e.g., year-day 45 and 293 in 2008) and multiple spectral peaks due to swell and turning winds (discussed below). For sustained wind forcing, the spectral peak may remain approximately constant at lower frequencies as the waves reach a fully developed wind-wave equilibrium sea states (Phillips, 1985) (e.g., around year-day 263). However, a relatively constant low-frequency peak in the spectrum may also indicate nonequilibrium remote swell waves (e.g., year-day 192–202). Secondary spectral peaks develop when the wind turns and the waves adjust to the changing wind direction, resulting in complex swell sea states (e.g., year-day 47). In summary, these observations and simulations clearly indicate that the sea state on the shelf is complex and that the wave field is rarely in equilibrium with the wind forcing.

3.1.3. Importance of Nonequilibrium Sea States

A common feature in the time series of $\phi_1(f)$ is the frequency downshift followed by the appearance of a secondary peak in ϕ_1 (e.g., year-day 45 in 2008). Such features are associated with complex sea states due to turning winds. To show this, we examine the simulated two-dimensional wave height spectrum ϕ_2 during a period from year-day 45 to 46 in 2008 (starting at 13 February 2008 00:00 UTC) (Figure 6). Here θ is the wave propagation direction and $\phi_2(f,\theta)$ is defined such that $\phi_1(f)=\int_0^{2\pi}\phi_2(f,\theta)d\theta$. Initially, the wind blows steadily at $U_{10}\approx 7$ m/s toward north-west and the spectrum increases and frequencies become smaller during wave growth. The black line separates the wind-forced part of the spectrum for which $c/[U_{10}\cos(\Delta\theta)] \leq 1.2$, where $c(f)$ is the phase speed at f using the linear dispersion relation, and $\Delta\theta=\theta-\theta_w$ is the difference between θ and the wind direction θ_w. At 13 February 2008 18:00 UTC, the wind vector (red line, Figure 6) rotates clockwise and has completed an approximate 180° turn at 14 February 2008 at 02:00 UTC after which the wind remains fairly constant at $U_{10}\approx 7.5$ m/s. During and after the turning wind event, relatively long waves that were initially in equilibrium with the wind forcing persist and become swell waves, characterized by the narrow spectral low-frequency peak that opposes the wind direction.

The wind vector and ϕ_2 with the condition $c/[U_{10}\cos(\Delta\theta)] \leq 1.2$ for wind-forced waves provide a rational approach to partition the wave spectrum into swell and wind-forced parts (Portilla et al., 2009). To systematically assess the importance of swell and wind-driven seas, we partition ϕ_2 at the Shelf location (NDBC 44009) for the full year 2008 into swell and wind-forced parts and compute wave statistics for each part (Figure 7). We discuss here only the simulation results at this Shelf location because the wave and wind forcing are similar over the shelf and results for other locations on the shelf sufficiently away from the coast do not differ substantially.

As expected, H_s for the wind-driven spectrum (Figure 7a) is consistent with the wind forcing dominantly from S (~180°) and NW (~315°) (Figure 7d). Waves from E to S (90−180°) are predominantly swell waves (Figure 7c) and likely generated remotely outside our domain (compare with wave forcing at the boundary, Figure 7g). For waves with $H_s > 0.5$ m, swell waves contribute substantially to overall wave energy (Figure 7e). Sufficiently fast long-period waves are not forced by the wind and, consequently, the mean period $T_m=\langle\eta^2\rangle/\int_0^\infty f\,\phi_1(f)df$ of swell waves exceeds the one of wind-driven waves (Figure 7f). Consistent with the distributions of peak periods discussed above, our results suggest that a wave field with $T_m < 3$ s is likely wind-driven, whereas $T_m > 5$ s likely indicates the dominant presence of a swell waves. Our results reveal the ubiquitous

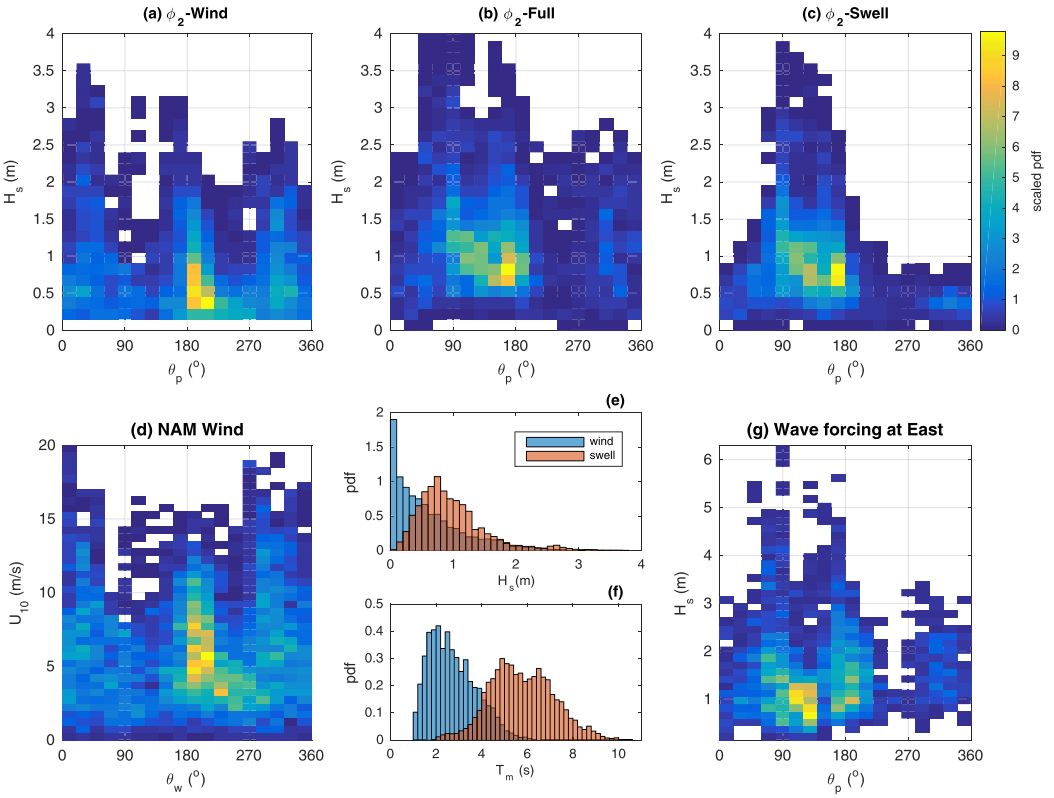

Figure 7. Probability density functions based on the partitioning analysis of simulated wind-forced $\phi_2(f,\theta)$ at NDBC 44009 (Shelf). The pdfs of H_s and θ_p are for the (a) wind-forced ϕ_2, (b) full ϕ_2, (c) swell ϕ_2, which are compared to the pdf of (d) the forcing wind vector and (g) the wave boundary forcing. The pdfs of (e) H_s and (f) T_m differ significantly for wind and swell waves.

presence of swell waves and complex sea states on the shelf, which must be taken into account for accurate modeling of surface waves propagating over the shelf near Delaware's coastal regions.

3.1.4. Note on Wave-Current Interactions

Our results indicate that ocean currents influence average wave statistics only relatively weakly compared to the influence of wind forcing and swell. For example, the root mean square difference between H_s of the default coupled run and of a run without coupling to ocean currents is only about 0.2 m, i.e., much less than typical mean H_s of about 1.5 m. It is important to note, however, that our statistical analysis approach is not aimed at revealing the effects of local current events, which could still critically influence local wave dynamics. For example, converging currents in river plume fronts on the shelf may focus wave energy and locally enhance wave breaking (Thomson et al., 2009; Zippel & Thomson, 2017). Our statistical wave analysis may still provide insights into the effects of currents if the spatiotemporal current structure is relatively regular, such as for strong tidal currents in Delaware Bay, which is discussed below.

3.1.5. Wave Propagation From Shelf to Bay

To investigate wave propagation from the shelf into the bay, we focus on refraction due to bathymetry because waves are expected to be refracted away from the deep channel. Note that one might anticipate an analogous refraction effect due to flooding tidal currents if they extend sufficiently outside the bay mouth. However, our model results suggest that bathymetric refraction is more important in sheltering the bay from open ocean waves and that refraction effects by currents can be complicated because the refraction characteristics are sensitive to the detailed horizontal distributions of currents (see section 3.2.4).

We design idealized stationary wave simulations that are only forced at the open boundaries with a prescribed constant empirical JONSWAP spectrum (Hasselmann et al., 1973) and specified H_s, T_p, and spectral peak direction θ_p. These idealized wave simulations do not include wind forcing or ocean currents. Guided by our previous results (Figure 4), we set a typical T_p to $T_p = 6$ s and a longer period swell T_p to $T_p = 12$ s. Consistent with typical wave boundary forcing conditions, we set $\theta_p = 70°, 130°$, and $180°$. The significant wave height is not a critical parameter for swell propagation and arbitrarily set to $H_s = 1$ m.

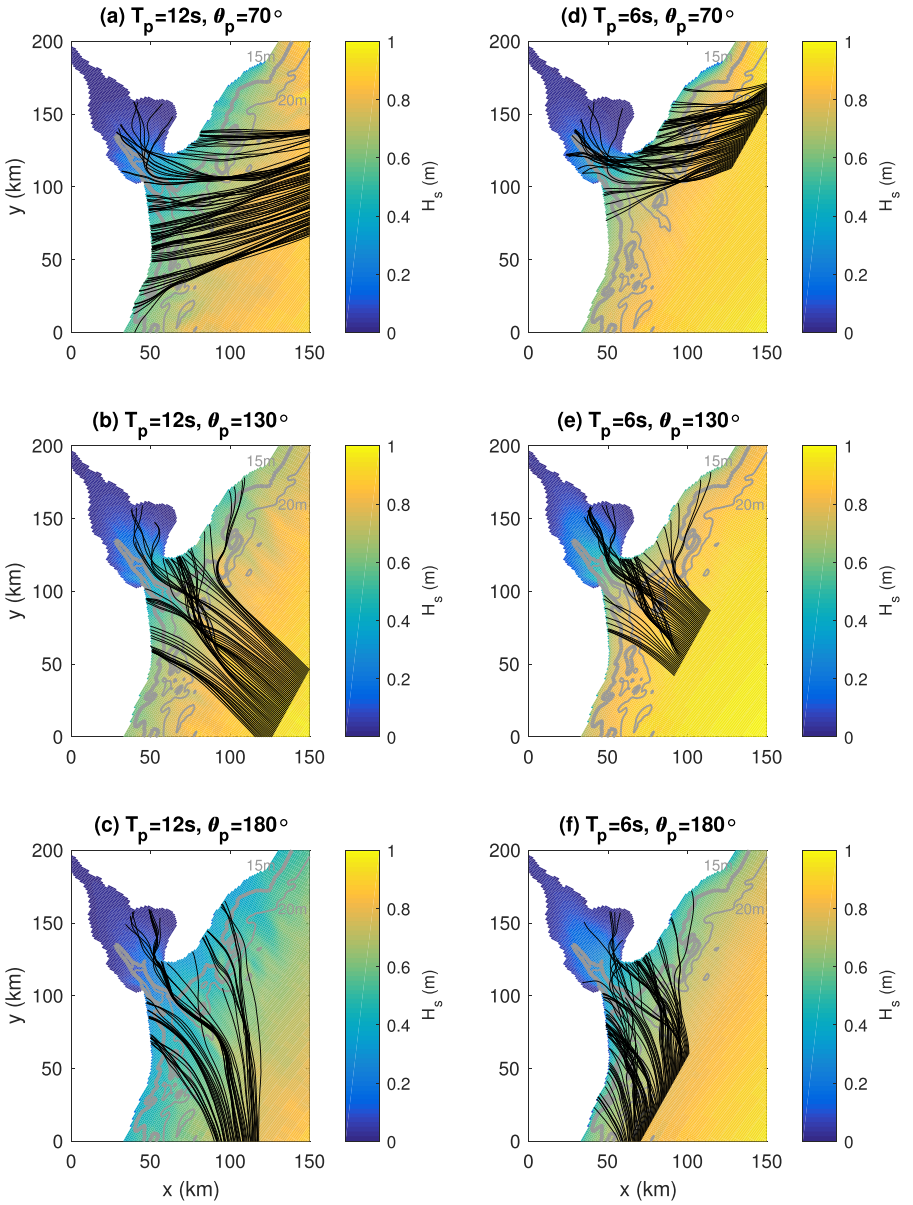

Figure 8. Delaware Bay is sheltered from swell waves that are generated remotely outside the Bay. The colors show simulated significant wave height (H_s) of idealized swell waves (without coupling to ocean currents) that are specified at the open boundaries of the model by their angle of incidence θ_p and peak period T_p with $H_s = 1$ m. Incident wave rays (black lines), which are determined from ray tracing theory for corresponding θ_p and T_p for monochromatic waves, are strongly refracted or blocked by land.

To understand spatial sheltering and refraction, we also implement complementary wave ray tracing experiments based on the conservation of wave crests in a body of water with slowly varying depth (Mei et al., 2005). Following Mei et al. (2005), the wave ray path $y(x)$ is given

$$\frac{d}{dx}\left(\frac{ky'}{[1+y'^2]^{1/2}}\right)=(1+y'^2)^{1/2}\frac{\partial k}{\partial y}, \tag{1}$$

where $y'=dy/dx$ is the ray slope and k is the wavenumber governed by the linear dispersion relation of surface gravity waves. Equation (1) is solved for different initial positions, slopes, and wave periods using standard (fourth-order Runge-Kutta method) numerical ordinary differential equation solvers; the longitudinal coordinate x and latitudinal coordinate y are swapped if the slope exceeds a threshold. These idealized ray

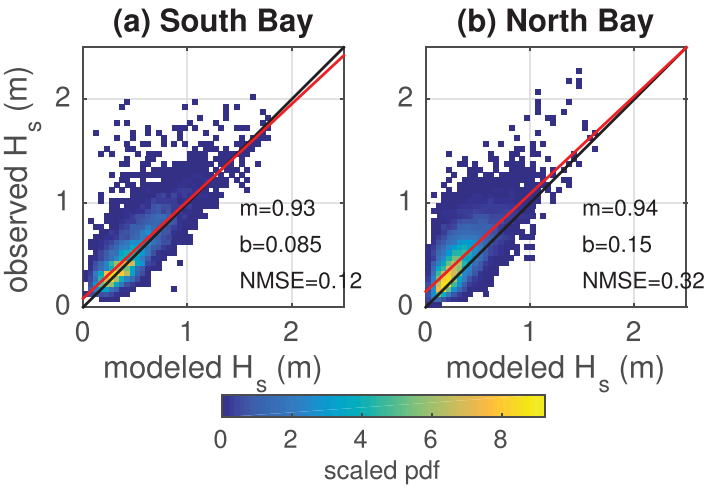

Figure 9. Linearly scaled probability density function (pdf) of observed H_s ($H_{s,o}$) versus modeled ($H_{s,m}$) for all available data between 2006 and 2012 at (a) S Bay and (b) N Bay, 1:1 line (black), and linear regression fit $H_{s,o}=mH_{s,m}+b$ (red line, units of b are in meter).

tracing solutions isolate effects of bathymetric refraction on wave propagation and, thus, greatly facilitate the interpretation of the complex SWAN model solutions.

Both the idealized swell simulations and the ray tracing experiments show that remotely generated swell waves are not capable of deeply propagating into Delaware Bay (Figure 8). The ray tracing results reveal that refraction plays a key role in sheltering the bay, as wave rays turn into and out the deep channel to reach the shore before deeply propagating into the bay. As expected, refraction is stronger for larger T_p, so that the Delaware Bay is likely protected from energetic long wave swell generated by remote storms. These results also indicate an interplay between refraction and land obstacles. For example, wave rays can curve around Cape May (North at the bay entrance) to reach the northern shore in New Jersey. Except near the southern shore at the bay entrance, wave rays are less likely to reach the southern Delaware shore. In summary, bathymetric refraction overall shelters the bay from energetic surface gravity waves from the shelf.

3.2. Wave Dynamics in the Bay

3.2.1. Overview

As for the shelf analysis, we first examine seasonal wave statistics to provide an overview of wave dynamics in response to the seasonal forcing (Figure 2). Largest mean H_s occurs during the autumn and winter seasons with mean values of 0.6 m in bay. During winter, H_s in the bay is greater because winds are stronger during this season. This differs from the shelf results, highlighting that the bay is relatively sheltered from larger shelf swell waves, as discussed in the previous subsection. Consistent with the relatively weak wind forcing, smallest mean H_s in the bay is found during summer with H_s smaller than 0.5 m. Spring H_s in the bay is consistent with the relatively moderate wind and wave boundary forcing during this period. In the bay, T_p ranges between 2 s (upper bay) and 6 s (near the mouth) with relatively weak seasonal variability. Near the bay's deep channel, T_p is relatively small, which indicates that longer waves are refracted by the deep channel bathymatry.

Compared to the shelf, mean $|\Delta\theta_p|$ in the bay is smaller for all seasons with values less than 30° in the upper bay, indicating locally generated wind waves and the sheltering of the bay against swell from the shelf. The branched patterns of $|\Delta\theta_p|$ inside the bay and $|\Delta\theta_p|$ gradients along the coast are due to wave refraction. Mean $|\Delta\theta_p|$ in the bay is larger in regions near the bay mouth for the autumn, summer, and spring months with values exceeding 45°. This suggests some swell influence at the mouth of the bay. The spring, summer, and autumn seasons have similar swell probabilities with typical values of $P_s < 50\%$ except near the bay mouth. As on the shelf, swell probability is lower in the winter than for the other seasons with values in the bay well below 40%, consistent with wind-driven seas during winter.

3.2.2. Comparison of Observations and Simulations

A direct comparison reveals reasonable agreement between observed and modeled H_s (Figure 9). The NMSE values are greater in the bay than on the shelf, which is expected because the wind vector is less accurate in the bay. In particular, the NAM wind product does not capture details of small-scale wind variability in the upper bay (Hughes & Veron, 2015). Significantly smaller simulated H_s occurs during observed short-lived high wind events that the NAM wind does not capture. For example, for observed $H_s \approx 2$ m, but modeled $H_s < 0.5$ m (Figure 9), we find a NAM $U_{10}=3$ m/s and observed $U_{10}=15$ m/s. However, such extreme differences in model and observed winds are rare as the pdf in Figure 9 indicates. The NAM product captures larger scale mean wind fields, so that on average modeled significant wave height agree reasonably well with observations. Again it is important to keep in mind that the model and forcing data have been taken as is based on straightforward and common approaches without any tuning to enhance model performance; given this, the agreement is surprisingly good.

Simulated and observed time-dependent one-dimensional wave height frequency spectra $\phi_1(f)$ are also consistent and illustrate the wave response to variable wind forcing conditions (Figure 10). Observations contain spurious low-frequency peaks for $f < 0.1$ s^{-1} (not shown in Figure 10), which is not related to wave dynamics but due to low-frequency accelerometer noise that is amplified as f^{-4} in ϕ_1. This peak prevents

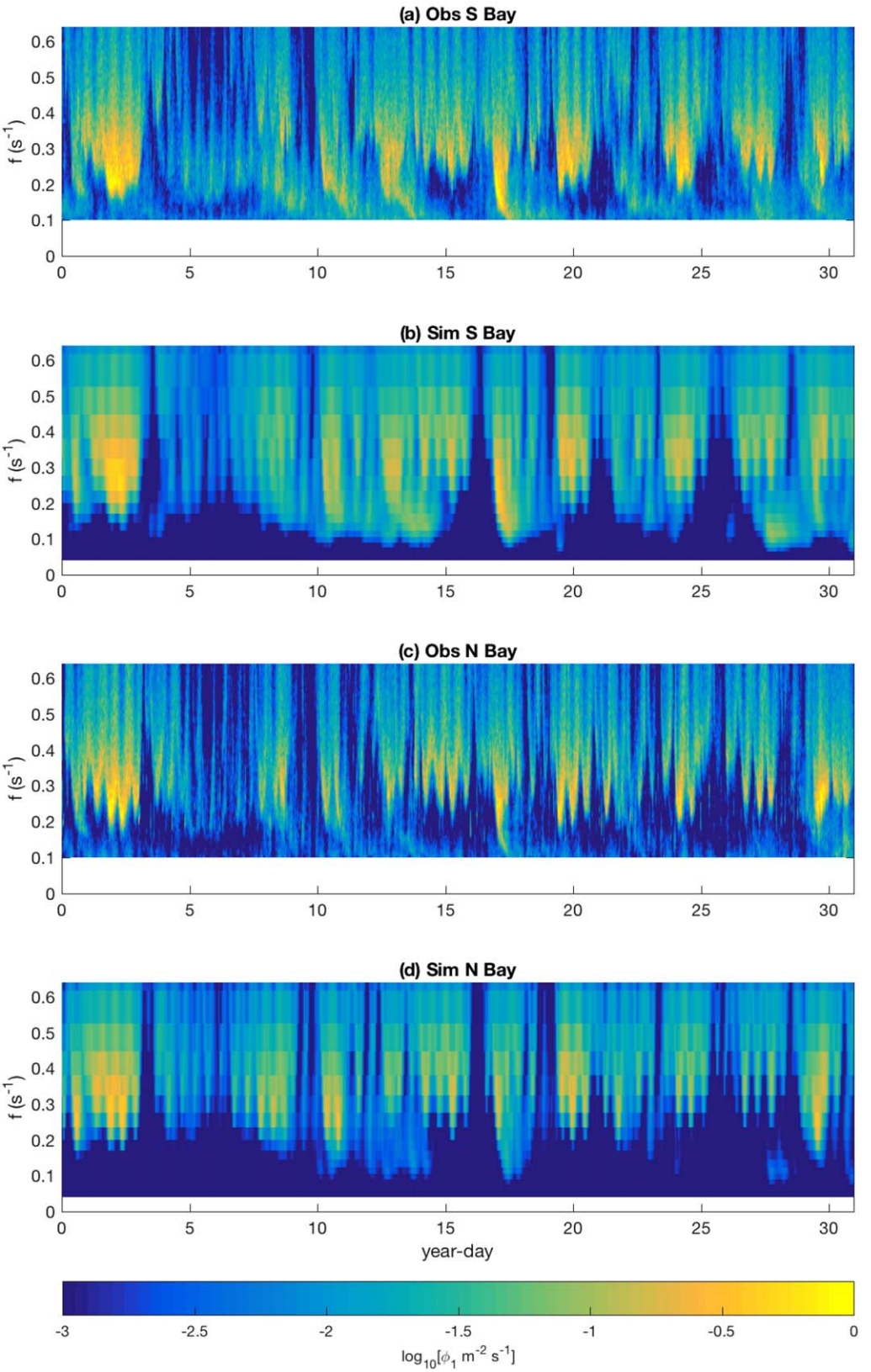

Figure 10. (a, c) Observed and (b, d) simulated $\phi_1(f)$ at (a, b) S Bay and (c, d) N Bay. Note that observed spurious low-frequency content for $f < 0.1$ s^{-1} due to low-frequency accelerometer noise is not shown (see main text).

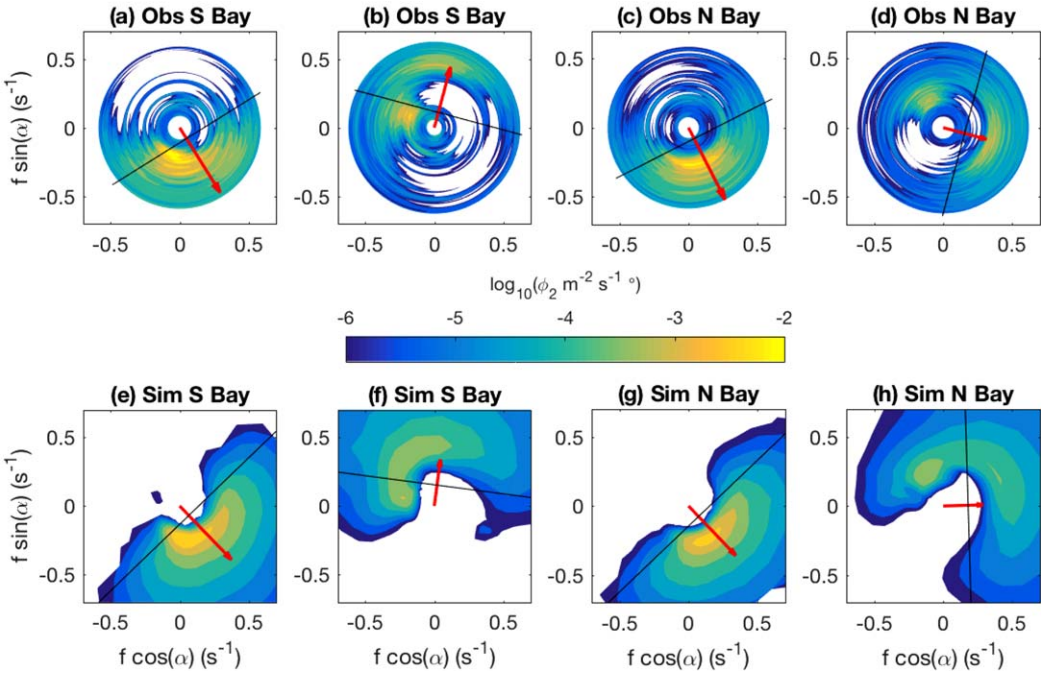

Figure 11. Example of (a–d) observed and (e–h) simulated $\phi_2(f,\theta)$ at (left plots) S Bay and (right plots) N Bay during January 2008. The black line separates the wind-forced part of the spectrum for which $c/[U_{10}\cos(\Delta\theta)] \leq 1.2$. The red line indicates the wind vector with magnitude of (a, c, e, g) about $U_{10}=13$ m/s for a steady strong wind case and (b, d, f, h) about $U_{10}=7$ m/s for a turning wind case. The wave propagation direction $\alpha=270^{\circ}-\theta$ uses Cartesian convention.

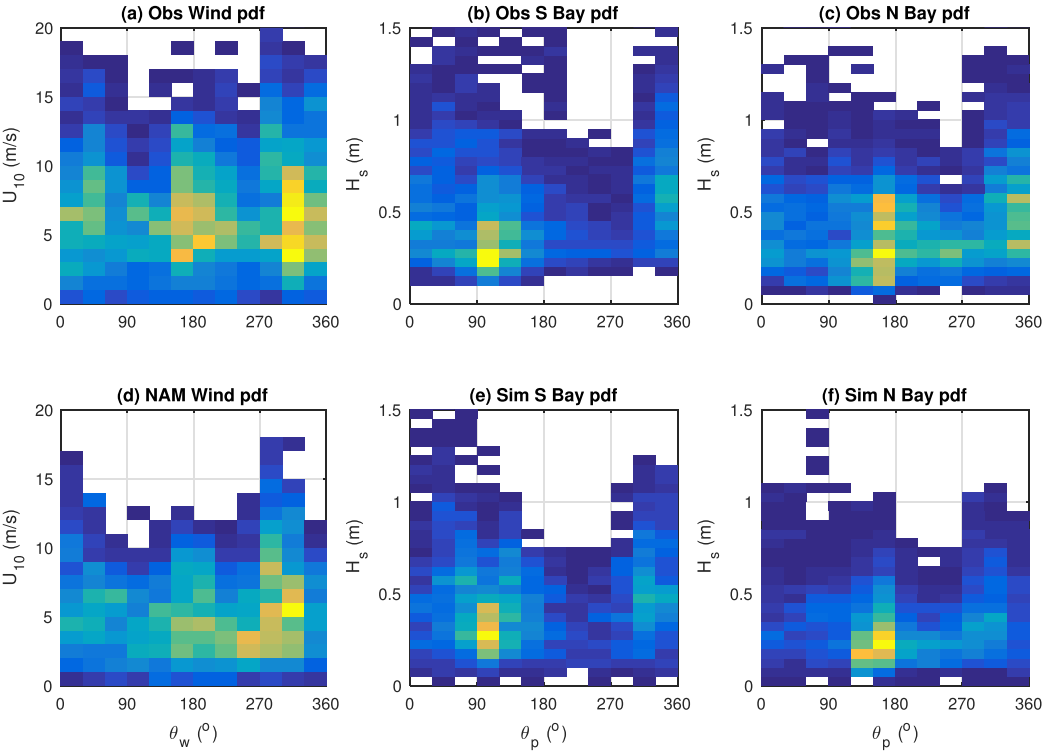

Figure 12. (a–c) Observed and (d–f) simulated directional pdfs for (a, d) U_{10} and (b, c, e, f) H_s at (b, e) S Bay and (c, f) N Bay. Colorbar as in Figure 9.

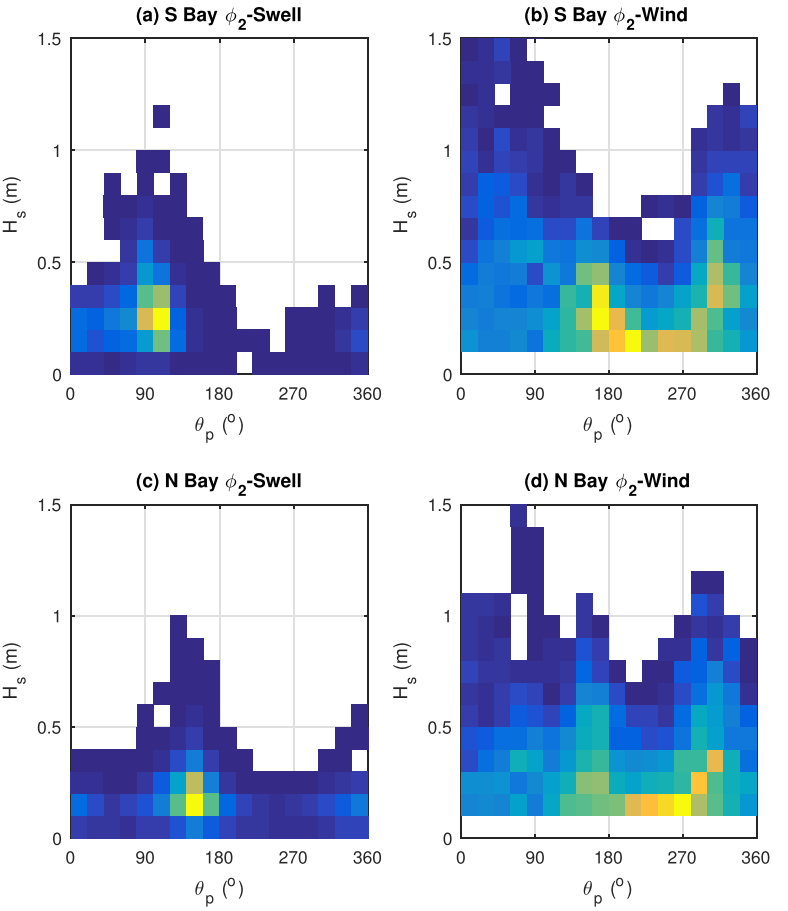

Figure 13. Probability density functions based on the partitioning analysis of simulated $\phi_2(f,\theta)$ at (a, b) S Bay and (c, d) N Bay. The pdfs of H_s and θ_p are for (b, d) the wind-forced ϕ_2 and (a, c) the swell ϕ_2. Colorbar as in Figure 9.

us from confidently estimating peak frequencies in low wind conditions, when spectral levels are small, but does not otherwise significantly influence the analyses presented here, because its contribution to $\langle \eta^2 \rangle$ is small. Spectral frequency downshift and multiple spectral peaks are also observed and simulated at both bay locations, but these features are less pronounced than on the shelf because fetch-limited bay waves quickly develop and swell is less important. The structure of ϕ_1 is more complex at S Bay because this location is more influenced by waves propagating from the open ocean. Another marked difference from the shelf results is the semidiurnal oscillations of the peak frequency due to interactions with tidal currents as discussed in detail in section 3.2.4.

As expected based on results for H_s and ϕ_1, observed and simulated two-dimensional wave height spectra $\phi_2(f,\theta)$ agree qualitatively well (Figure 11). Differences in the detailed spectral distributions are expected due to errors and resolution limitations of the wind forcing. Typical examples for similar model and observation wind conditions are shown in Figure 11 for S Bay (plots a, b, e, and f) and N Bay (plots c, d, g, and h). The first example illustrates the response to a fairly steady wind vector (red line), displaying the misalignment between wind and spectral peak direction due to refraction (Figures 11a, 11c, 11e, and 11g). The straight black line, which separates the part of the wave spectrum that is directly forced by the wind from the part that is not forced by the wind (see above), indicates dominantly wind-driven seas because most of the spectral wave energy is directly forced by the wind. Generally, however, bay winds are highly variable and may change abruptly in magnitude or direction. The second example shows an instant during the transient wave response to such unsteady winds (Figures 11b, 11d, 11f, and 11h). Rapidly turning winds result in a secondary spectral peak with older swell waves that are not forced by the wind, which highlights that wave characteristics in the bay cannot always be simply scaled with the instantaneous wind vector.

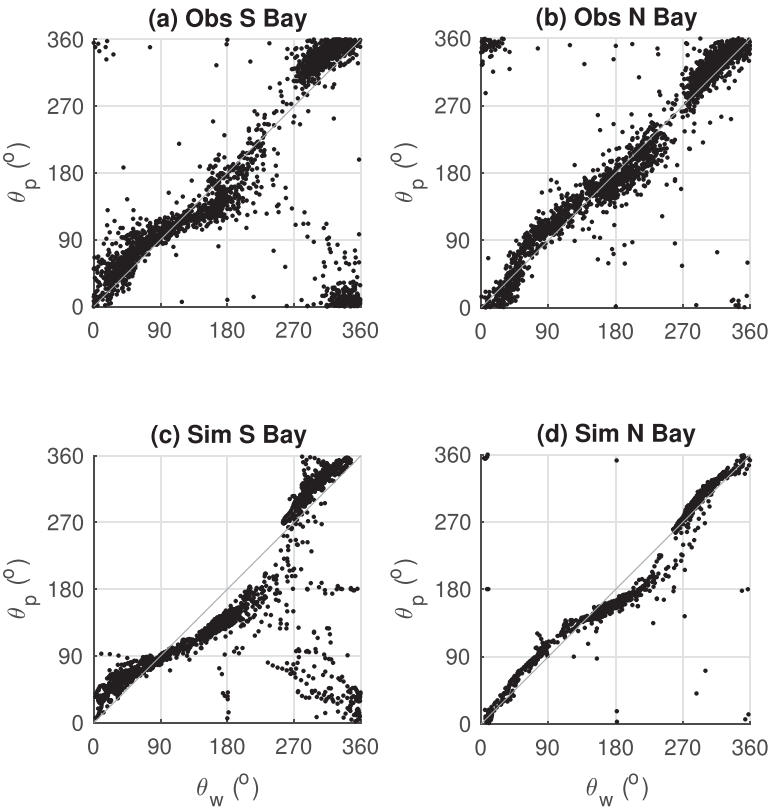

Figure 14. (a, b) Observed and (c, d) simulated θ_p versus θ_w for (a, c) South Bay and (b, d) North Bay.

Observed and simulated directional pdfs of H_s are consistent (Figures 12b, 12c, 12e, and 12f), displaying a primary peak for low $H_s < 0.5$ m for waves from about E (90°) at S Bay and from about S (180°) at N Bay. At S Bay, this peak is not consistent with the wind forcing pdfs (Figures 12a and 12d), indicating the presence

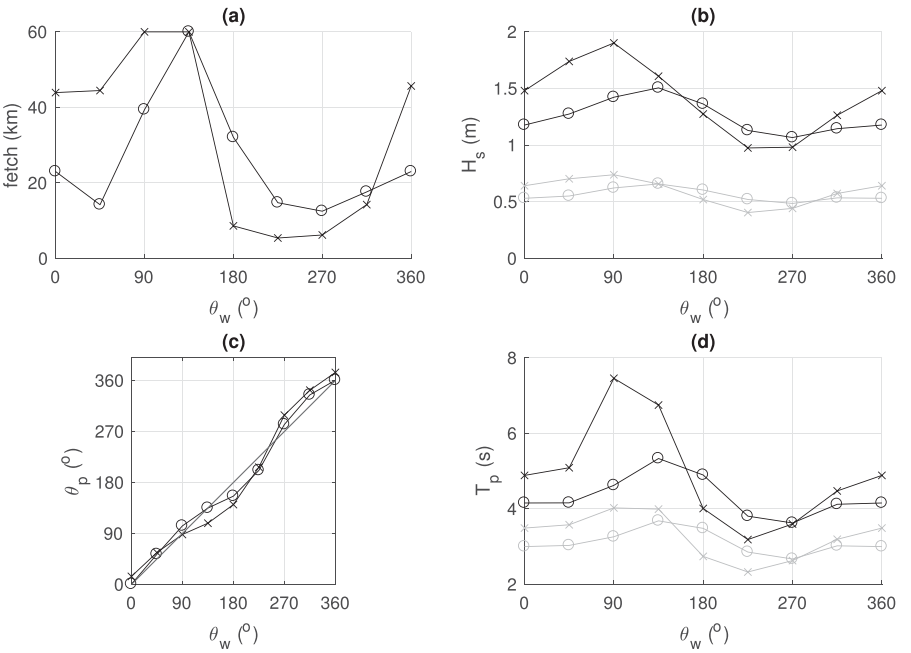

Figure 15. Dependence of (a) fetch, (b) H_s, (c) θ_p, and (d) T_p on θ_w at S Bay (cross) and N Bay (circle). The wind vector is constant with $U_{10}=8$ m/s (gray) and $U_{10}=15$ m/s (black).

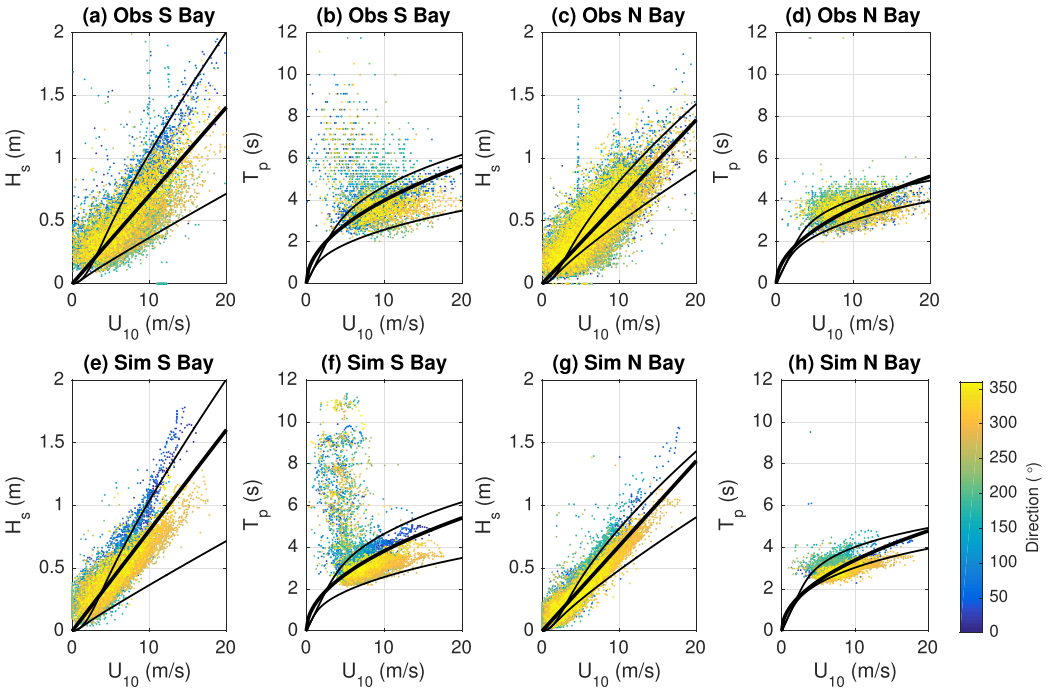

Figure 16. (top plots) Observed and (bottom plots) simulated H_s and T_p for South (left plots) and North Bay (right plots). Color coding indicates wind direction. Only instances with $H_s > 0.5$ m are included (see main text). Thick black line shows regression fits for $H_s = a_H U_{10}$ and $T_p = a_T U_{10}^{1/2}$. Thin black lines show empirical formulae from Young and Verhagen (1996) for great depth/long fetches at South Bay ($x_f = 60$ km, $h = 15$ m) and North Bay ($x_f = 60$ km, $h = 6$ m) and for shallow depth/short fetches at South Bay ($x_f = 6$ km, $h = 5$ m) and North Bay ($x_f = 13$ km, $h = 4$ m).

of low energy swell waves. Interestingly, the directions of the primary pdf peaks are consistent with wave propagation from the bay entrance without refraction, suggesting weak sources of wave energy from the shelf. A secondary peak in the pdf with dominant wave directions from between W and N approximately coincides with the wind forcing, indicating wind-driven seas.

3.2.3. Importance of Local Wind-Driven Waves

To systematically examine swell and wind seas in the bay, we apply the same partitioning analysis discussed in section 3.1.3, but performed on simulated $\phi_2(f, \theta)$ in the bay during the year 2008 (Figure 13). These results confirm that the primary peaks are from swell propagating from E at S Bay and from SE at N Bay. The analysis furthermore reveals two wind-driven peaks from S and NW consistent with the wind forcing (Figure 12d). At S Bay and for $H_s > 0.5$ m, the wind-driven part of ϕ_2 exceeds swell contributions to H_s by 81%, whereas for $H_s < 0.5$ m about 67% of the time the swell part of ϕ_2 contributes dominantly to H_s. At the

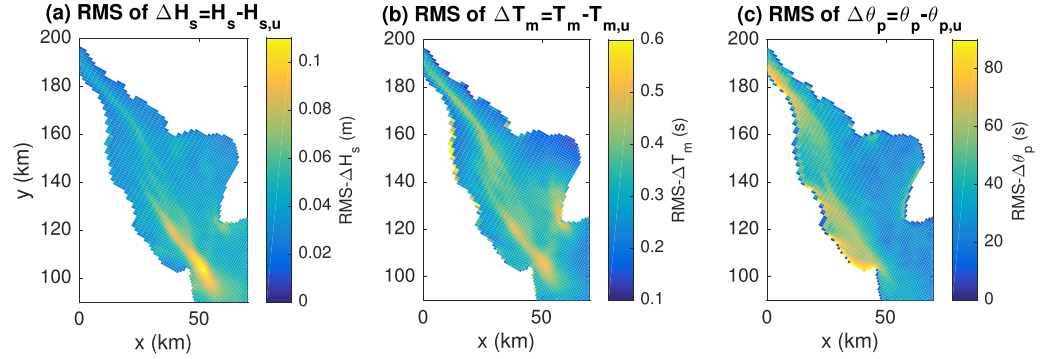

Figure 17. RMS differences of H_s, T_m, θ_p between coupled (default) and uncoupled runs (indicated by subscript u) for years 2007 and 2008 illustrate the typically small influence of tidal currents on bulk wave statistics.

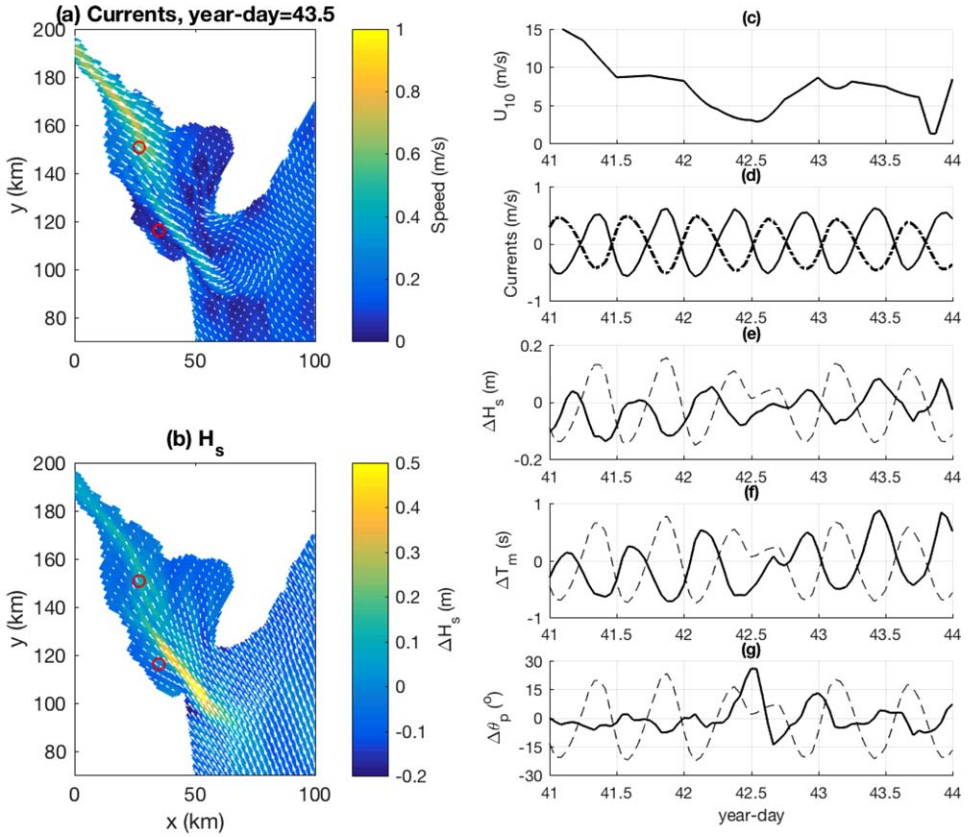

Figure 18. Example of collinear currents effects on wave dynamics: (a) current magnitude and direction (arrows), (b) difference of H_s between coupled and uncoupled runs and wave direction obtained from θ_p (arrows) for the coupled run. Corresponding time series at N Bay are shown for (c) wind speed, (d) eastward current (solid) and northward current (dash-dotted), (e) H_s, (f) T_m, and (g) θ_p differences between coupled and uncoupled runs. For reference, linearly scaled U_p is shown in Figures 18e–18g (dashed lines). Red circle shows location of N Bay and S Bay.

more sheltered N Bay location, swell waves are even less important with 93% wind-driven dominance for $H_s > 0.5$ m and only 51% swell dominance for $H_s < 0.5$. These results highlight that swell waves are ubiquitous in the bay if H_s is relatively small; however, energetic wave conditions are characterized by wind-driven seas. Therefore, the remaining part of this section focuses on wind-driven waves in the bay, which are estimated by the criterion $H_s > 0.5$ m based on the partitioning analysis.

The peak wave direction for fetch-limited and depth-limited wind waves is generally not aligned with the wind (Figure 14). This is expected not only because of refraction, but also because of changing wind direction, which introduces a directional bias toward directions with longer fetches (Donelan et al., 1985). Observations and simulations for $H_s > 0.5$ m indicate that wind and waves are only approximately aligned for angles around 90° and 270° (Figure 14). For winds from directions between about 90° and 270°, the wave propagation angle is smaller than the wind direction (waves propagate left to wind), while for winds from 0° to 90° or 270° to 360°, the wave propagation angle exceeds the wind angle (waves propagate right to wind). This pattern is consistent with both wave refraction, as wave rays bend toward shore, and the bay's fetch characteristics (Figure 15a). For example, directional variability of an average wind from S biases the wave directions toward E because of longer fetches from E.

To further examine the observed directional bias and fetch dependence of waves in the bay, we design idealized wave simulations with constant wind vector with $U_{10}=8, 15$ m/s and different wind directions (Figure 15). The results of the directional wave bias are consistent with the realistic simulations and observations and supports that refraction is a key factor for the observed wind wave misalignment. These results also highlight that wave characteristics, such as H_s (Figure 15b) and T_p (Figure 15d), are generally controlled by the wind direction, which determines the fetch, in particular at S Bay whose fetch is more variable with wind direction.

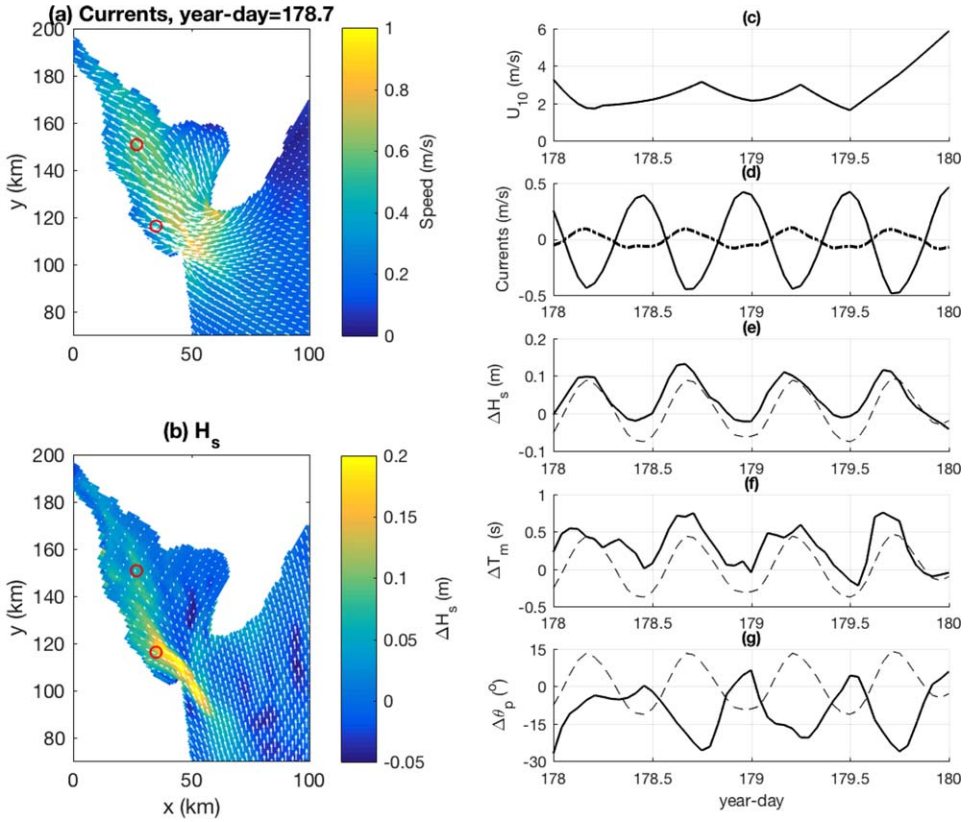

Figure 19. Example of wave refraction in low wind conditions: (a) current magnitude and direction (arrows), (b) difference of H_s between coupled and uncoupled runs and wave direction obtained from θ_p (arrows) for the coupled run. Corresponding time series at S Bay are shown for (c) wind speed, (d) eastward current (solid) and northward current (dash-dotted), (e) H_s, (f) T_m, and (g) θ_p differences between coupled and uncoupled runs. For reference, linearly scaled U_p is shown in Figures 19e–19g (dashed lines). Red circle shows location of N Bay and S Bay.

For wind-driven seas, the observed and simulated dependence of H_s and T_p on U_{10} agrees well in spite of significant scatter due to variable winds and swell (Figure 16). This scatter is greater for the observations, consistent with the greater variability of observed winds. The average response to U_{10} is estimated by linear regressions for $H_s = a_H U_{10}$ and $T_p = a_T U_{10}^{1/2}$, which are asymptotic expressions of empirical formulae for fetch-limited wave fields (e.g., Young & Verhagen, 1996) (thick black line, a_H, a_T are dimensional linear regression coefficients). At S Bay, H_s and T_p are greater for winds from E (90°) which is consistent with larger fetches from those directions (compare with Figure 15a). Peak periods exceeding 5 s at S Bay indicate the presence of swell waves from the open ocean, which contribute to the scatter in Figures 16b and 16f. At N Bay, T_p and H_s are less scattered and depend less on wind direction, which is expected because the fetch varies less with wind direction. The magnitude of H_s and T_p are roughly consistent with previous observations of depth and fetch dependent wind-driven waves, which have been parameterized by empirical formulae (Young & Verhagen, 1996) (thin black lines in Figure 16). For the lower bound of the empirical H_s and T_p, we assume the smallest depth h and shortest fetch x_f ($x_f = 6$ km, $h = 5$ m for S Bay and $x_f = 13$ km, $h = 4$ m for N Bay), while for the upper bound, we assume the greatest h and longest x_f ($x_f = 60$ km, $h = 15$ m for S Bay and $x_f = 60$ km, $h = 6$ m for N Bay). In spite of this consistency, our results indicate that refraction and remotely generated swell waves generally need to be taken into account for a complete analysis of wave dynamics in Delaware Bay, even for wind-driven waves.

3.2.4. Influence of Tidal Currents

Our analysis focuses on the typical influence of strong tidal currents in the bay, as explained in section 3.1.4. The substantial wave response to wind forcing (section 3.2.3) and its high-frequency variability makes it generally challenging to determine the relatively weak current influence. Note that tidal currents also change the effective local wind speed and direction and, thus, the wind forcing on waves. However, this

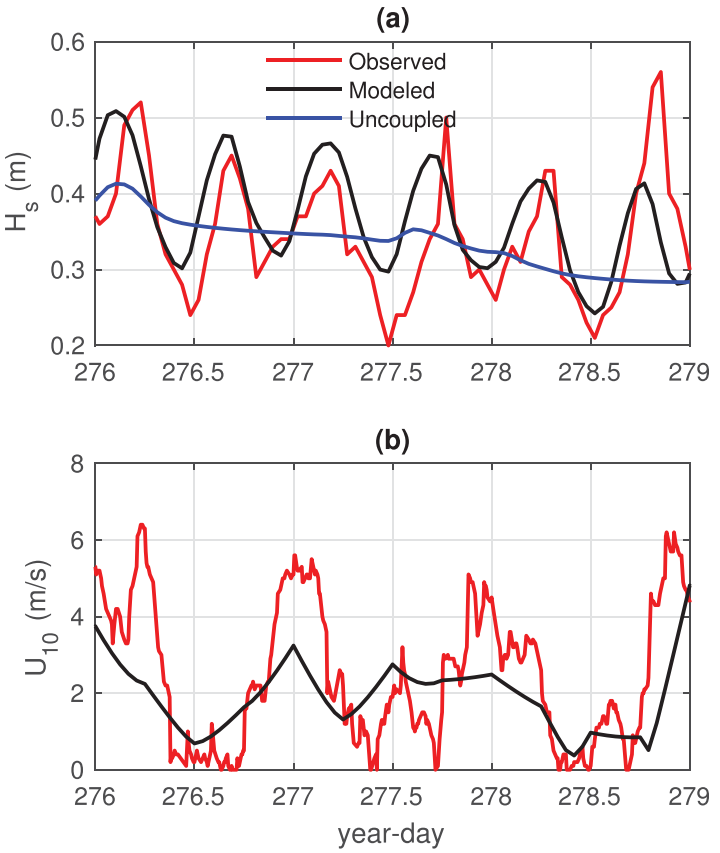

Figure 20. (a) Observed and simulated modulations of H_s by tidal currents in low wind conditions at the South Buoy. (b) High-frequency variability of U_{10} and the strong wave response to wind forcing generally make it challenging to observe such current modulations.

current effect is weak if the current speed is much smaller than U_{10} and if the exposure of waves to stronger currents along the deeper bay channels is relatively short (see Figures 1 and 13).

Tides also drive water level changes, which generally changes refraction characteristics. However, tidal elevation changes slowly and the tidal amplitude is usually much smaller than the water depth, so that tidal elevation does not predominantly modulate wave dynamics in Delaware Bay. To test this, we designed sensitivity experiments in which the wave model is only coupled to water levels. The results of these experiments are, indeed, very close to the uncoupled simulation results.

To cleanly separate wind from current effects, we perform additional wave simulations without coupling to the ocean circulation model for years 2007 and 2008. The root mean square (RMS) differences between coupled and uncoupled runs of H_s, T_m, and θ_p clearly indicate that waves are modulated by ocean currents (Figure 17). Relatively large RMS values for H_s and T_m are colocated with deeper channels in the bay (compare with Figure 1), where currents are strong (typical currents are shown in Figures 18a and 19a). Variability of H_s due to tidal currents is expected because converging currents along the wave propagation direction focus wave energy and diverging currents spread wave energy (e.g., Mei et al., 2005). Relatively large variations of wave period in strong current regions are anticipated because currents Doppler shift the intrinsic wave frequency. Interestingly, the RMS of the θ_p difference is particularly large near the western shore of the bay, which indicates wave refraction by currents. Waves that propagate obliquely to horizontally sheared currents are refracted, which either focuses or spreads wave energy depending on the shear direction and the incidence angle of the waves on the currents. Because of this directional dependence and because the refraction characteristics depend on wave period, refraction by currents also affects wave period and H_s.

We will next examine scaling expectations for modulations of H_s and wave period due to collinear currents (an example is shown in Figure 18). Conservation of wave action yields for the amplitude A of a wave train propagating on a collinear current (e.g., Mei et al., 2005)

$$\left(\frac{A}{A_0}\right)^2 = \frac{\sigma}{\sigma_0}\frac{c_{g0}}{c_g + U_p}, \tag{2}$$

where U_p denotes the current velocity projected into the wave propagation direction. The subscript zero indicates a reference location without currents, $A = 8^{-1/2}H_s$ represents the amplitude of a monochromatic wave with intrinsic group velocity c_g and intrinsic wave frequency σ obtained from the linear dispersion relation. For a typical tidal current amplitude of 0.7 m/s and a typical wave period of 4 s (compare Figure 2), equation (2) yields for deep water waves variations of H_s between -18% and $+33\%$ over a tidal cycle, which is close to our model results (Figures 17 and 18). The wave period modulation due to the Doppler shift kU_p is for 4 s wave periods and $U_p = \pm 0.7$ m/s about ± 0.5 s, which approximately agrees with our results (Figures 17 and 18) and explains the semidiurnal modulations of $\phi_1(f)$ observed in Figure 10. We found the largest increase and decrease in H_s of about 0.5 m (40% change compared to the uncoupled simulations) in 2008 during relatively stormy conditions with $U_{10} > 12$ m/s, when ebbing currents focused waves propagating from south-east and reduced wave eights of waves from north-west. During these extreme events, the relative distributions of currents and changes in H_s due to currents resemble the current distribution shown in Figure 18 and the RMS difference of H_s (Figure 17), respectively, suggesting the importance of collinear current effects.

Wave refraction by currents is more challenging to assess analytically because refraction characteristics are highly sensitive to the spatial distributions of the sheared currents and the wave incidence angles.

Furthermore, refraction effects by currents may interact with refraction by bathymetry. Let us consider an example during flooding tidal currents to illustrate such complicated, perhaps nonintuitive, refraction characteristics. During flooding tidal currents, one may expect that waves outside the bay are refracted toward the sides analogous to bathymetric refraction due to the deep channel, reducing wave energy in the bay. However, we find that waves outside the bay from S may be turned into the bay during flooding tidal currents and energy is subsequently focused as waves exit regions of strong currents (Figure 19). Unlike the effect of collinear currents, in this case, U_p correlates with H_s and wave period (Figures 19e and 19f). The differences in θ_p between coupled and uncoupled runs clearly indicate that wave rays from S are bent into the bay by current refraction. We find observational evidence for such wave modulations in low wind conditions (Figure 20), but a more comprehensive analysis will need to disentangle relatively weak current effects and obscuring dominant wind effects. Furthermore, for a direct comparison between simulations and observations, it is critical that the wind forcing in the model includes observed high-frequency variability.

4. Discussions and Conclusions

Based on a systematic analysis of wave simulations and observations during a period from 2006 to 2012, this study provides a broad overview of surface gravity wave dynamics in Delaware Bay and its adjacent continental shelf. Building on previous approaches, simulation results are obtained from a coupled application of the Regional Ocean Modeling System (ROMS, Haidvogel et al., 2000; Shchepetkin and McWilliams, 2005) and Simulating Waves Nearshore (SWAN, Booij et al., 1999; SWAN Team, 2007, 2009) within the Coupled-Ocean-Atmospheric-Wave-Sediment Transport (COAWST) modeling framework (Warner et al., 2010). Both models are forced by NAM analyses wind products. Realistic wave boundary conditions are imposed at the open oceanic boundaries based on archived WaveWatchIII simulation results. We have validated the model with observations from three wave buoys located on the shelf about 50 km south-east from the bay entrance (NDBC station 44009), south in the bay near the open ocean (NDBC station 44054), and about 35 km up the bay (NDBC station 44055).

Overall, distributions of simulated significant wave heights, peak wave periods peak wave directions, and wave height frequency spectra agree well with observations. A direct comparison for events, however, is less successful because of spatiotemporal resolution limitations of the wind forcing applied in the models. Observations and simulations are also qualitatively consistent, revealing the relative importance of locally generated wind-waves, remotely generated swell waves, bathymetric wave refractions, and wave modulations by ocean currents.

Significant wave height, peak period, misalignment angle, and swell probability strongly depend on the seasonal cycle because the wind forcing also depends on season. Largest significant wave heights are found during autumn and winter when winds are stronger. The lowest peak period occurs during winter, which is consistent with relatively low swell probabilities and small misalignment angles during winter, indicating a more pronounced wind-driven sea during winter. Consistent with the relatively weak wind forcing, smallest mean significant wave heights in the bay occur during the summer.

A partitioning analysis to separate the two-dimensional wave height spectrum into wind-forced and swell parts reveals that waves on the shelf are usually not in equilibrium with the local wind forcing, but the wave field is characterized by remotely generated swell. Furthermore, transient and turning winds result in complex sea states with multiple spectral peaks. These results suggest that wave properties on the shelf generally do not scale with the instantaneous wind forcing, which has important implications for parameterizing wave-driven circulation (e.g., Lentz & Fewings, 2012), upper ocean turbulence (e.g., Kukulka et al., 2012), and air-sea fluxes (e.g., Sullivan et al., 2008).

Because of bathymetric refraction and obstruction by land, the propagation of longer waves from the shelf into the bay is impeded, which is supported by our idealized ray tracing analysis. This results in an effective sheltering of the bay from larger shelf waves. Those few wave rays that are guided into the bay reach most likely parts of the northern lower Delaware Bay shore. Interestingly, this part of the shore coincides with regions of enhanced shoreline erosion rates (Pijanowski & Sommerfield, 2015), indicating the importance of wave processes in coastal erosion processes in Delaware Bay. In reality, strong bathymetric refraction generally also causes wave diffraction and leakage of wave energy into the bay (Kirby & Dalrymple, 1983; Thomson et al., 2005), which our wave models do not accurately capture.

Surface gravity waves from the shelf are also refracted by tidal currents to substantially modulate wave amplitudes in the bay near the bay entrance. Refraction effects on waves due to horizontally sheared currents interact with wave energy focusing effects due to converging currents, particularly near the bay entrance. The magnitude of typical wave height and period modulation by strong tidal currents in the relatively deep channel in the bay are consistent with wave action conservation for waves propagating on collinear currents. Both simulated and observed frequency wave height spectra show characteristic Doppler shifts due to strong tidal currents. Furthermore, our study indicates that it is generally more challenging to observe wave energy modulations due to currents because high-frequency wind variability often drives changes in wave energy in the bay, obscuring the influence of tidal currents. It is also important to keep in mind that a simplified approach has been employed to represent vertically sheared currents in the wave model (Kirby & Chen, 1989). Recent research suggests that this approach should be reconsidered and improved, particularly in environments with strongly sheared flows (Banihashemi et al., 2017).

A partitioning analysis for bay wave height spectra indicates that only small waves with significant wave heights below about 0.3 m are not dominantly forced by the wind. Larger waves, one the other hand, are likely directly forced by the wind and the wave response in the bay depends on wind direction, which sets the fetch. For wind-driven bay waves, our results are consistent with previous fetch-limited observations, but we find a systematic bias between wind and wave directions due to bathymetric refraction. Thus, this study indicates that the largest waves observed in the upper bay are likely generated by local storms over the bay.

Acknowledgments
Funding was supported by the Shoreline and Waterway Management Section, Delaware Department of Natural Resources and Environmental Control, by the University of Delaware Research Foundation, and by the National Science Foundation award OCE-1634578. This research was supported in part through the use of computational or staff resources provided by Information Technologies at the University of Delaware. We would like to thank Philip Orton for stimulating discussions and suggestions. Two anonymous reviewers provided valuable comments that have substantially improved this paper. All models and data used in this paper are open access and can be obtained as described in detail in section 2 of this paper.

References

Akan, Ç., Moghimi, S., Özkan-Haller, H. T., Osborne, J., & Kurapov, A. (2017). On the dynamics of the mouth of the Columbia River: Results from a three-dimensional fully coupled wave-current interaction model. *Journal of Geophysical Research: Oceans*, *122*, 5218–5236. https://doi.org/10.1002/2016JC012307

Ardhuin, F., Chapron, B., & Collard, F. (2009). Observation of swell dissipation across oceans. *Geophysical Research Letters*, *36*, L06607. https://doi.org/10.1029/2008GL037030

Ardhuin, F., O'reilly, W. C., Herbers, T. H. C., & Jessen, P. F. (2003). Swell transformation across the continental shelf. Part I: Attenuation and directional broadening. *Journal of Physical Oceanography*, *33*(9), 1921–1939.

Aristizábal, M., & Chant, R. (2013). A numerical study of salt fluxes in Delaware Bay estuary. *Journal of Physical Oceanography*, *43*(8), 1572–1588.

Baker, A. J., Gonzalez, P. M., Piersma, T., Niles, L. J., Lima Serrano do Nascimento, I., Atkinson, P. W., . . . Aarts, G. (2004). Rapid population decline in red knots: Fitness consequences of decreased refuelling rates and late arrival in Delaware Bay. *Proceedings of the Royal Society of London B: Biological Sciences*, *271*(1541), 875–882. https://doi.org/10.1098/rspb.2003.2663

Banihashemi, S., Kirby, J. T., & Dong, Z. (2017). Approximation of wave action flux velocity in strongly sheared mean flows. *Ocean Modelling*, *116*, 33–47. https://doi.org/10.1016/j.ocemod.2017.06.002

Booij, N., Ris, R., & Holthuijsen, L. (1999). A third-generation wave model for coastal regions 1. Model description and validation. *Journal of Geophysical Research*, *104*, 7649–7666.

Botton, M. L., Loveland, R. E., & Jacobsen, T. R. (1988). Beach erosion and geochemical factors: Influence on spawning success of horseshoe crabs (*Limulus polyphemus*) in Delaware Bay. *Marine Biology*, *99*(3), 325–332.

Brown, H. C., & Scarborough, R. W. (2013). Wave data analysis in the Delaware Bay. In *2013 OCEANS-San Diego* (pp. 1–5). San Diego, CA: IEEE Xplore. Retrieved from http://ieeexplore.ieee.org/document/6740995/

Castellano, P., & Kirby, J. (2011). *Validation of a hydrodynamic model Delaware Bay and the adjacent coastal region* (Res. Rept. CACR-11-03). Newark, DE: Center for Applied Coastal Research, University of Delaware.

Cavaleri, L., Alves, J.-H., Ardhuin, F., Babanin, A., Banner, M., Belibassakis, K., . . . Young, I. (2007). Wave modelling—The state of the art. *Progress in Oceanography*, *75*(4), 603–674. https://doi.org/10.1016/j.pocean.2007.05.005

Chen, J., Ralston, D., Geyer, W., Chant, R., & Sommerfield, C. (2016). Characteristics of wind generated waves in the Delaware estuary. In *Abstract (EC14C-1014) presented at 2016 Ocean Sciences Meeting, AGU/ASLO/TOS, New Orleans, LA, 21-27 Feb*. Retrieved from https://agu.confex.com/agu/os16/preliminaryview.cgi/Paper93685.html

Chen, Y., Shi, Qin, F. W., & Kirby, J. T. (2008). Coupling of meteorology, ocean, and nearshore models for predicting coastal inundation along Delaware's coast. In *10th international conference on estuarine and coastal modeling* (pp. 150–162), Newport, RI.

Craik, A. D. D., & Leibovich, S. (1976). A rational model for Langmuir circulations. *Journal of Fluid Mechanics*, *73*, 401–426.

Donelan, M. A., Hamilton, J., & Hui, W. H. (1985). Directional spectra of wind-generated waves. *Philosophical Transactions of the Royal Society of London, Series A*, *315*, 509–562.

Elgar, S., & Guza, R. (1985). Observations of bispectra of shoaling surface gravity waves. *Journal of Fluid Mechanics*, *161*, 425–448.

Gargett, A. E., Wells, J., Tejada-Martinez, A. E., & Grosch, C. E. (2004). Langmuir supercells: A mechanism for sediment resuspension and transport in shallow seas. *Science*, *306*, 1925–1928.

Gerbi, G. P., Trowbridge, J. H., Terray, E. A., Plueddemann, A. J., & Kukulka, T. (2009). Observations of turbulence in the ocean surface boundary layer: Energetics and transport. *Journal of Physical Oceanography*, *39*(5), 1077–1096.

Haidvogel, D. B., Arango, H. G., Hedstrom, K., Beckmann, A., Malanotte-Rizzoli, P., & Shchepetkin, A. F. (2000). Model evaluation experiments in the north Atlantic basin: Simulations in nonlinear terrain-following coordinates. *Dynamics of Atmospheres and Oceans*, *32*(3), 239–281.

Hanley, K. E., Belcher, S. E., & Sullivan, P. P. (2010). A global climatology of wind-wave interaction. *Journal of Physical Oceanography*, *40*, 1263–1282. https://doi.org/10.1175/2010JPO4377.1

Hara, T., & Belcher, S. E. (2002). Wind forcing in the equilibrium range of wind-wave spectra. *Journal of Fluid Mechanics*, *470*, 223–245.

Hasselmann, K. (1970). Wave-driven inertial oscillations. *Geophysical Fluid Dynamics*, *1*(3–4), 463–502. https://doi.org/10.1080/03091927009365783

Hasselmann, K., Barnett, T., Bouws, E., Carlson, H., Cartwright, D., Enke, K., . . . Walden, H. (1973). Measurements of wind-wave growth and swell decay during the Joint North Sea Wave Project (JONSWAP). *Deutsche Hydrographische Zeitschrift Supplement*, *8*(12), 95.
Herbers, T., & Burton, M. (1997). Nonlinear shoaling of directionally spread waves on a beach. *Journal of Geophysical Research*, *102*, 21101–21114.
Herbers, T., Hendrickson, E., & O'reilly, W. (2000). Propagation of swell across a wide continental shelf. *Journal of Geophysical Research*, *105*, 19729–19737.
Hofmann, E. E., D., Bushek, S. E., Ford, X., Guo, D., Haidvogel, D., Hedgecock, J. M., . . . Zhang, L. (2009). Understanding how disease and environment combine to structure resistance in estuarine bivalve populations. *Oceanography*, *22*(4), 212–231.
Holthuijsen, L. H. (2010). *Waves in oceanic and coastal waters*. Cambridge, UK: Cambridge University Press.
Hughes, C., & Veron, D. (2015). Characterization of low-level winds of southern and coastal Delaware. *Journal of Applied Meteorology and Climatology*, *54*(1), 77–93. https://doi.org/10.1175/JAMC-D-14-0011.1
Jenkins, R. L. III (2015). *Surface wave analysis based on a hydrodynamic modeling system for the Delaware coastal environment* (Master's thesis). Newark, DE: University of Delaware.
Johnson, J. (1947). The refraction of surface waves by currents. *Eos Transactions American Geophysical Union*, *28*(6), 867–874.
Jurisa, J. T., & Chant, R. J. (2013). Impact of offshore winds on a buoyant river plume system. *Journal of Physical Oceanography*, *43*(12), 2571–2587.
Kirby, J. T., & Chen, T.-M. (1989). Surface waves on vertically sheared flows: Approximate dispersion relations. *Journal of Geophysical Research*, *94*, 1013–1027.
Kirby, J. T., & Dalrymple, R. A. (1983). Propagation of obliquely incident water waves over a trench. *Journal of Fluid Mechanics*, *133*, 47–63. https://doi.org/10.1017/S0022112083001780
Komen, G. J., Cavaleri, L., Donelan, M., Hasselmann, K., Hasselmann, S., and Janssen, P. A. E. M. (Eds.) (1996). *Dynamics and modelling of ocean waves* (1st ed., 532 pp.). Cambridge, UK: Cambridge University Press.
Kraft, J. C., Yi, H.-L., & Khalequzzaman, M. (1992). Geologic and human factors in the decline of the tidal salt marsh lithosome: The Delaware estuary and Atlantic coastal zone. *Sedimentary Geology*, *80*(3), 233–246. https://doi.org/10.1016/0037–0738(92)90043-Q
Kukulka, T., & Hara, T. (2008). The effect of breaking waves on a coupled model of wind and ocean surface waves: II. Growing seas. *Journal of Physical Oceanography*, *38*(10), 2164–2184.
Kukulka, T., Plueddemann, A. J., & Sullivan, P. P. (2012). Nonlocal transport due to Langmuir circulation in a coastal ocean. *Journal of Geophysical Research*, *117*, C12007. https://doi.org/10.1029/2012JC008340
Kumar, N., Feddersen, F., Uchiyama, Y., McWilliams, J., & O'reilly, W. (2015). Midshelf to surfzone coupled ROMS-SWAN model data comparison of waves, currents, and temperature: Diagnosis of subtidal forcings and response. *Journal of Physical Oceanography*, *45*(6), 1464–1490. https://doi.org/10.1175/JPO-D-14–0151.1
Large, W., & Pond, S. (1981). Open ocean momentum flux measurements in moderate to strong winds. *Journal of Physical Oceanography*, *11*(3), 324–336.
Lentz, S. J., & Fewings, M. R. (2012). The wind-and wave-driven inner-shelf circulation. *Annual Review of Marine Science*, *4*, 317–343.
Longuet-Higgins, M. S. (1953). Mass transport in water waves. *Philosophical Transactions of the Royal Society of London A: Mathematical, Physical and Engineering Sciences*, *245*(903), 535–581. https://doi.org/10.1098/rsta.1953.0006
Longuet-Higgins, M. S., & Stewart, R. (1964). Radiation stresses in water waves: A physical discussion, with applications. *Deep Sea Research and Oceanographic Abstracts*, *11*(4), 529–562. https://doi.org/10.1016/0011–7471(64)90001-4
Luettich, R. A., Jr., Westerink, J. J., & Scheffner, N. W. (1992). *Adcirc: An advanced three-dimensional circulation model for shelves, coasts, and estuaries. Report 1. Theory and methodology of ADCIRC-2DDI and ADCIRC-3DL* (Tech. Rep. DRP-92-6, 137 pp.). Vicksburg, MS: Coastal Engineering Research Center.
McWilliams, J. C., Restrepo, J. M., & Lane, E. M. (2004). An asymptotic theory for the interaction of waves and currents in coastal waters. *Journal of Fluid Mechanics*, *511*, 135–178. https://doi.org/10.1017/S0022112004009358
Mei, C. C., Stiassnie, M., & Yue, D. K.-P. (2005). *Advanced series on ocean engineering: Volume 23, theory and applications of ocean surface waves, Part 1: Linear aspects* (1st ed., 513 pp.). Princeton, NJ: World Scientific.
Mellor, G. L. (2008). The depth-dependent current and wave interaction equations: A revision. *Journal of Physical Oceanography*, *38*(11), 2587–2596.
Melville, W. K. (1996). The role of surface-wave breaking in air-sea interaction. *Annual Review of Fluid Mechanics*, *28*, 279–321.
Münchow, A., Masse, A. K., & Garvine, R. W. (1992). Astronomical and nonlinear tidal currents in a coupled estuary shelf system. *Continental Shelf Research*, *12*(4), 471–498.
Munk, W. H., Miller, G. R., Snodgrass, F. E., & Barber, N. F. (1963). Directional recording of swell from distant storms. *Philosophical Transactions of the Royal Society of London. Series A, Mathematical and Physical Sciences*, *255*(1062), 505–584.
Peregrine, D. (1976). Interaction of water waves and currents, *Advances in Applied Mechanics*, *16*, 9–117.
Phillips, J. (1986). Spatial analysis of shoreline erosion, Delaware Bay, New Jersey. *Annals of the Association of American Geographers*, *76*, 50–62.
Phillips, O. (1958). The equilibrium range in the spectrum of wind-generated waves. *Journal of Fluid Mechanics*, *4*, 426–434.
Phillips, O. (1977). *The dynamics of the upper ocean* (2nd ed., 336 pp.). Cambridge, UK: Cambridge University Press.
Phillips, O. (1985). Spectral and statistical properties of the equilibrium range in wind-generated gravity waves. *Journal of Fluid Mechanics*, *156*, 505–531.
Pijanowski, K., & Sommerfield, C. (2015). Historical shoreline change in Delaware estuary, Paper presented at the 2015 Coastal Research Federation Meeting, 8–12 November 2015, Portland, OR.
Portilla, J., Ocampo-Torres, F., & Monbaliu, J. (2009). Spectral partitioning and identification of wind sea and swell. *Journal of Atmospheric and Oceanic Technology*, *26*(1), 107–122. https://doi.org/10.1175/2008JTECHO609.1
Qin, W., Kirby, J. T., & Badiey, M. (2005). *Application of the spectral wave model SWAN in Delaware Bay* (Res. Rept. CACR-05–09). Newark, DE: Center for Applied Coastal Research, University of Delaware.
Rodrigues, A. P. F. (2016). *Hydrodynamic modeling of Delaware Bay with applications to storm surges and coastal flooding: Current conditions and future scenarios* (Master's thesis). Newark, DE: University of Delaware.
Romero, L., & Melville, W. K. (2010). Airborne observations of fetch-limited waves in the gulf of tehuantepec. *Journal of Physical Oceanography*, *40*(3), 441–465.
Schmalz, R. A. (2011). *Skill assessment of the Delaware River and Bay Operational Forecast System (DBOFS)*. Silver Spring, MD: U.S. Department of Commerce, National Oceanic and Atmospheric Administration, National Ocean Service, Office of Coast Survey, Coast Survey Development Laboratory.
Scully, M. E., Fisher, A. W., Suttles, S. E., Sanford, L. P., & Boicourt, W. C. (2015). Characterization and modulation of Langmuir circulation in Chesapeake Bay. *Journal of Physical Oceanography*, *45*(10), 2621–2639. https://doi.org/10.1175/JPO-D-14–0239.1

Semedo, A., Suselj, K., Rutgersson, A., & Sterl, A. (2011). A global view on the wind sea and swell climate and variability from era-40. *Journal Climate*, *24*, 1461–1479. https://doi.org/10.1175/2010JCLI3718.1

Sharp, J. H. (1983). *The Delaware estuary: Research as background for estuarine management and development*. Newark, DE: University of Delaware and New Jersey Marine Sciences Consortium.

Shchepetkin, A. F., & McWilliams, J. C. (2005). The regional oceanic modeling system (ROMS): A split-explicit, free-surface, topography-following-coordinate oceanic model. *Ocean Modelling*, *9*(4), 347–404.

Smith, J. A. (2006). Wave-current interactions in finite depth. *Journal of Physical Oceanography*, *36*(7), 1403–1419. https://doi.org/10.1175/JPO2911.1

Smith, R. (1976). Giant waves. *Journal of Fluid Mechanics*, *77*(3), 417–431.

Sullivan, P. P., Edson, J. B., Hristov, T., & McWilliams, J. C. (2008). Large-eddy simulations and observations of atmospheric marine boundary layers above nonequilibrium surface waves. *Journal of the Atmospheric Sciences*, *65*(4), 1225–1245.

Sullivan, P. P., & McWilliams, J. C. (2010). Dynamics of winds and currents coupled to surface waves. *Annual Review of Fluid Mechanics*, *42*, 19–42. https://doi.org/10.1146/annurev-fluid-121108–145541

SWAN Team (2007). *Swan user manual*. Delft, the Netherlands: Delft University of Technology.

SWAN Team (2009). *Swan technical documentation*. Delft, the Netherlands: Delft University of Technology.

Thomson, J., Elgar, S., & Herbers, T. H. C. (2005). Reflection and tunneling of ocean waves observed at a submarine canyon. *Geophysical Research Letters*, *32*, L10602. https://doi.org/10.1029/2005GL022834

Thomson, J., Gemmrich, J. R., & Jessup, A. T. (2009). Energy dissipation and the spectral distribution of whitecaps. *Geophysical Research Letters*, *36*, L11601, https://doi.org/10.1029/2009GL038201

Thorpe, S. A. (2004). Langmuir circulation. *Annual Review of Fluid Mechanics*, *36*, 55–79. https://doi.org/10.1146/annurev.fluid.36.052203.071431

Tolman, H. L. (1990). *Wind wave propagation in tidal seas, Communications on hydraulic and geotechnical engineering* (PhD thesis, 180 pp.). Delft, the Netherlands: Delft University of Technology.

Trowbridge, J., & Madsen, O. S. (1984). Turbulent wave boundary layers: 2. Second-order theory and mass transport. *Journal of Geophysical Research*, *89*, 7999–8007.

Umlauf, L., & Burchard, H. (2003). A generic length-scale equation for geophysical turbulence models. *Journal of Marine Research*, *61*, 235–265.

Warner, J. C., Armstrong, B., He, R., & Zambon, J. B. (2010). Development of a coupled ocean-atmosphere-wave-sediment transport (COAWST) modeling system. *Ocean Modelling*, *35*(3), 230–244.

Whitney, M. M., & Garvine, R. W. (2005). Wind influence on a coastal buoyant outflow. *Journal of Geophysical Research*, *110*, C03014. https://doi.org/10.1029/2003JC002261

Whitney, M. M., & Garvine, R. W. (2006). Simulating the Delaware Bay buoyant outflow: Comparison with observations. *Journal of Physical Oceanography*, *36*(1), 3–21.

Wong, K.-C., & Münchow, A. (1995). Buoyancy forced interaction between estuary and inner shelf: Observation. *Continental Shelf Research*, *15*(1), 59–88.

Young, I., & Verhagen, L. (1996). The growth of fetch limited waves in water of finite depth. Part 1. Total energy and peak frequency. *Coastal Engineering*, *29*(1), 47–78. https://doi.org/10.1016/S0378–3839(96)00006-3

Zavala-Garay, J., Wilkin, J., & Levin, J. (2014). Data assimilation in coastal oceanography: IS4DVAR in the Regional Ocean Modeling System (ROMS). In E. Blayo, M. Bocquet, E. Cosme and L. Cugliandolo (Eds.), *Advanced data assimilation for Geosciences Lecture Notes of the Les Houches School of Physics 2012* (pp. 555–576). Oxford, UK: Oxford University Press.

Zippel, S., & Thomson, J. (2017). Surface wave breaking over sheared currents: Observations from the mouth of the Columbia River. *Journal of Geophysical Research: Oceans*, *122*, 3311–3328. https://doi.org/10.1002/2016JC012498